Study on Nonlinearity and Applications in Integrated Silicon Photonics Devices

by

Hongcheng Sun

A dissertation submitted to The Johns Hopkins University in conformity with the requirements for the degree of Doctor of Philosophy.

Baltimore, Maryland

July, 2018

Abstract

With the exponential growth of data traffic in telecommunication, electrical interconnects based on copper traces and wires are nearly achieving the limitation of data transmission bandwidth requirements, and optical interconnects become extremely enticing due to the highly broad transmission bandwidth. Silicon integrated photonics has the potential to highly increase the data transmission bandwidth by developing on-chip optical interconnects and devices. Silicon photonics offers the main advantage of the compatibility of the mature complementary metal-oxide-semiconductor (CMOS) nano-fabrication technology.

The first chapter of this dissertation will discuss the background and three different silicon based platforms: crystalline silicon (c-Si), hydrogenate amorphous silicon (a-Si:H) and silicon nitride (Si_3N_4). Secondly, based on these three different material platforms, I will discuss five different demonstrations including (1) phase-sensitive amplification demonstration in a-Si:H waveguides, (2) Mid-IR supercontinuum generation in a-Si:H waveguides, (3) optical frequency combs in high-Q silicon nitride ring resonators, (4) photonic physical unclonable functions using silicon nitride spiral

waveguides and (5) compressed sensing of sparse RF signals based on silicon microdisk. Finally, I will discuss the conclusion and future work.

Primary Reader and Advisor: Prof. Amy C. Foster

Secondary Reader: Prof. Mark. A. Foster

Acknowledgments

This thesis would not be possible without continuous supports from my advisor, my dissertation committee, my family and friends. I want to express my deepest gratitude and thanks to them.

First and foremost, I would like to thank my advisor, Prof. Amy C. Foster for her guidance and financial support. As a great advisor and researcher, Amy always enlightens me with her knowledge in integrated nonlinear optics and device fabrication. Amy gives her students exceptional freedom in their research, and she is incredibly patient with me and supports me to deal with all the difficulties during my PhD study. Without her patience and persistence, the achievement make in this dissertation would not come true. I am also impressed by her passion for science and research as well as her unconditional love to her family.

I also would like to thank Prof. Mark A. Foster. He is always full of novel and interesting ideas, and he is also excellent with all kinds of skills and knowledge in optical experiments and ultra-fast optics. His insight make many demonstration of my fabricated photonic device possible. I am also profoundly grateful to his guidance

and advices during our closest collaboration.

I would like to thank my GBO committee: Prof. Xinde Li, Prof. James Spicer, Prof. Theodore Poehler and Prof. Jacob Khurgin. They all provided interest questions and discussions, which inspired me greatly in my following research study. Especially I would like to thank Prof. Jacob Khurgin, who is not only an exceptional theorist , but also an outstanding instructor and a friend. He also provide me a CA position to his Advanced Semiconductor course. His unique remarks make his courses and our study life a lot of fun.

I am thankful to my previous and current lab-mates in Integrated Photonics Lab: Ke-yao Wang, Kangmei Li, Michael Kossey, Brian Grubel and Neil MacFarlane for their help during my study. Particularly, I want to thank one previous member, Dr. Ke-yao Wang, the first PhD student in our lab. He provided me a lot of guidances and help and is incredibly patent with me. He also shows me a successful pathway to follow.

I also would like to thank collaborators from Ultrafast and Nonlinear Photonics Group: Bryan Bosworth, Hong-Fu Ting, Milad Alemohammad, Jaewook Shin, Jasper stroud and Iskandar Atakhodjaev for their help and close collaboration. Our group shared lab with them and we works together as a wonderful team.

Last but not least, I would like to thank my family: my wife Shanshan, my parents, grandparents, brothers and sisters. I would not be able to success without their unconditional love, support and companion. I would also like to thank all my

friends, who support me through my Ph.D study life.

I dedicate this thesis to my mom for nursing me with affections and supports. She dedicated partnership for any success in my life.

Contents

List of Tables

List of Figures

Chapter 1

Introduction

1.1 Integrated silicon photonics

During the past 40 years the processing speed of microprocessor has doubled every eighteen months, which is stated just as the famous Moore‘s Law [1]. With this exponential increase of microprocessors performance, electrical interconnects based on copper traces and wires are nearly achieving the limitation of data transmission bandwidth requirements, and optical interconnects become extremely enticing due to the highly broad transmission bandwidth.

Figure 1.1 presents the current market adoption of communication technology for different transmission distances. For long-haul transmission spanning 1-100 meters, well-developed optical fibers are already being used for optical interconnects. Fiber-optic communications has revolutionized the telecommunication community ever since

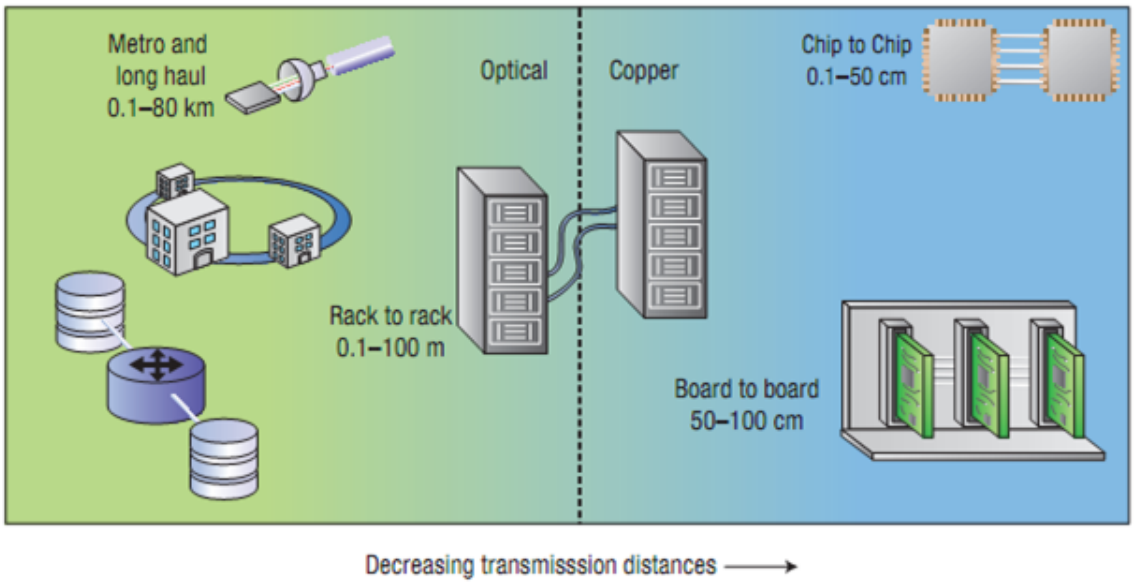

Figure 1.1: Current market adoption of communication technology for different transmission distances (from [2]).

the laboratory demonstration of laser in 1960s and the low loss optical fibers in 1970s. Till 1990s, fiber optical communication systems have evolved to a mature stage due to the availability of high-performance transmitter, optical fiber and receiver. For short transmission spanning less than 1 meter, such as board-to-board, chip-to-chip and on-chip, electrical interconnects are still dominant in the current status. However, there has attracted a huge interest from people to utilize optical interconnects for short range communication system for the past few decades. One potential solution is using integrated photonics to realize all optical interconnects on chip. With the development of integrated photonics, it is possible that optical links will ultimately take over for high speed data communication.

The success of microelectronics industry has made silicon photonics a promis-

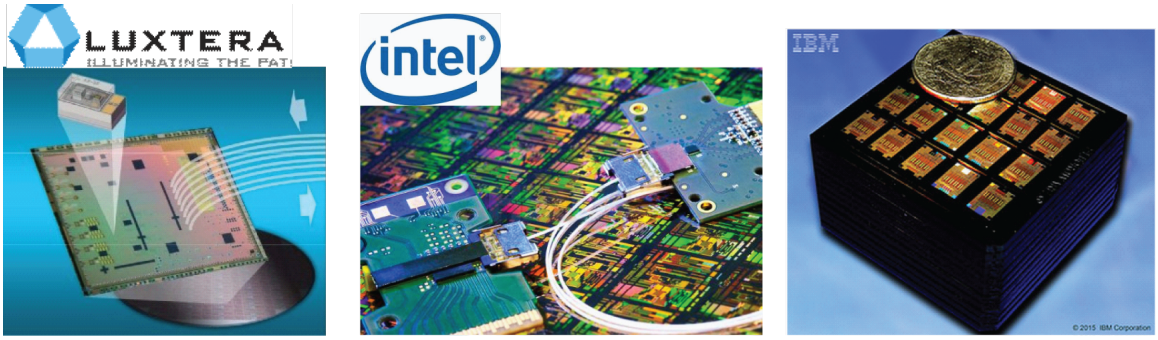

Figure 1.2: Three demonstrations of the integrated silicon circuits from Luxtera (from Luxtera website), Intel (from Intel website) and IBM (from IBM website).

ing device technology for optical communication in late 1980s. Silicon integrated photonics provide a potential solution by developing silicon based optical devices on chip [3]. The major advantage of silicon integrated photonics is the compatibility with the well-developed silicon microelectronics fabrication infrastructure, complementary metaloxidesemiconductor (CMOS) fabrication technology. The key driving force behind silicon photonics is the ability to use CMOS-like fabrication resulting in high-volume production at low cost. Within almost 40 years, a plethora of silicon photonic devices have been demonstrated and more complicated silicon photonic circuits are paving the way towards different applications. Though the development of silicon photonics was fueled by the telecommunication boom at early stage and it has shown its capability to fabricate various devices, it is important to fit these devices for different advanced communication systems. Figure 1.2 presents three demonstrations of the integrated silicon circuits from Luxtera, Intel and IBM. Luxtera has already shown a 100 Gbit/s optical transceiver chip based on silicon pho-

tonics. Intel has shown a fully integrated silicon photonic transmitter chip working at 50 Gb/s, it has hybrid silicon lasers and a fully integrated receiver chip based on germanium photodetectors. Recently, IBM has designed and tested a fully integrated wavelength multiplexed silicon photonics chip, which will soon enable manufacturing of 100 Gb/s optical transceivers. Cassette carrying several hundred chips intended for 100 Gb/s transceivers, diced from wafers fabricated with IBM CMOS Integrated Nano-Photonics Technology. This will allow datacenters to offer greater data rates and bandwidth forcloud computing and big data applications.

Silicon does however have a number of shortcomings as a photonic material. In its basic form it is not an ideal material in which to produce light sources, optical modulators or photodetectors for example. A wealth of research effort from both academia and industry in recent years has fueled the demonstration of multiple solutions to these and other problems, and as time progresses new approaches are increasingly being conceived. It is clear that silicon photonics has a bright future.

1.2 Nonlinear optics in silicon photonics

Nonlinear optics describes the behavior of light in nonlinear media, in which the dielectric polarization P responds nonlinearly to the electric field E of the light. In the case of conventional linear optics, the induced electric polarization $\tilde{\mathrm{P}}(\mathrm{t})$ is linearly proportional to the electric field strength $\tilde{E}(t)$ which can be described using this

equation:

$$\tilde{P}(t) = \epsilon_0 \chi^{(1))} \tilde{E}(t), \tag{1.1}$$

where the constant $\chi^{(1)}$ is known as the linear susceptibility. Actually, this equation has higher order terms and be expanded to the following equation,

$$\tilde{P}(t) = \epsilon_0 [\chi^{(1)} \tilde{E}(t) + \chi^{(1)} \tilde{E}^2(t) + \chi^{(2)} \tilde{E}^3(t) + \cdots]. \tag{1.2}$$

The quantities $\chi^{(2)}$ and $\chi^{(3)}$ are known as the 2nd-order and 3rd-order nonlinear optical susceptibilities, respectively. Higher order susceptibility can become prominent when the injecting light intensity is strong enough, and is particularly critical in very high confinement regimes such as integrated waveguides. Compared with the conventional linear optics, the major behavior differences between nonlinear optics and linear optics include:

(1) Refractive index of nonlinear medium is related to the optical intensity, which means the optical property of nonlinear medium can be changed by controlling the intensity of incident light.

(2) The frequency of incident light can be changed when the light is passing through a nonlinear medium, which means light at new frequencies can be generated when light is passing through a nonlinear medium.

(3) Two beam of light can interact with each other within a nonlinear medium and generate light at new frequencies, which means the ability to control light using light and the potential to realize all optical processing.

Moreover, the nonlinear optics process occurs usually in an ultra-fast scale about hundreds of tera-hertz and can be used for ultra-high speed signal processing. To note that, the 2nd-order nonlinear optical interactions can only occurs in noncentrosysmmetric crystals. On the other hand, 3rd-order nonlinear optical interaction can occurs in such structures. Most common CMOS-compatiable materials are centrosysmmetrical and no 2nd-order nonlinear optical interaction can occur. However, 3rd-order nonlinear optical interaction can occur in CMOS-compatiable materials and is very important.

The Kerr effect is a nonlinear optical effect that is related to 3rd-order nonlinearity. The Kerr effect is the effect of an instantaneously occurring nonlinear response, which can modify the refractive index by the high intensity of light beam. It is commonly written in this equation:

$$n = n_0 + n_2 I, \tag{1.3}$$

where n_2 is the nonlinear index and I is the optical intensity. The n_2 value of a medium is usually measured with the z-scan technique. As mentioned before, Kerr effect is related with 3rd-order nonlinearity, so the nonlinear index n_2 is related to

the real part of the 3rd-order nonlinear optical susceptibilities $\chi^{(3)}$ by the equation:

$$n_2 = \frac{3Re[\chi^{(3)}]}{8n} \tag{1.4}$$

From equation 1.3, we can see that silicon photonics is a great platform for nonlinear optics, n_2 in silicon is 2 orders of magnitude higher than optical fibers. Also, the dimension of the integrated waveguides is usually small, so the light will be better confined and has a highly enhanced intensity. So both two variables in the nonlinear term are enhanced, which makes silicon photonics well suitable for nonlinear optics applications.

1.3 Silicon based material platforms

Silicon photonics are firstly studied based upon crystalline silicon. Although crystalline silicon has a lot of good features such as high refractive index, high nonlinearity and abundant quantity on earth, there are other new materials which can also be compatible with the standard CMOS technology, such as amorphous silicon, poly silicon, silicon nitride, silicon rich siliocn nitride, even germanium and so on. These other materials keep the CMOS compatibility and have the ability to overcome some shortcoming of crystalline silicon or provide better performance. In the dissertation, other than crystalline siliocn, I will discuss two other materials: hydrogenate amorphous silicon and silicon nitride.

1.3.1 Crystalline silicon

The potential of integrated silicon photonics was recognized in 1985 in the first studies of crystalline waveguides [4,5], which are fabricated using silicon-on-insulator (SOI) wafers. This technique has attracted a great deal of attention and the commercialization started shortly after that in 1989 by Bookham Technology Ltd [6]. Silicon-on-insulator (SOI) is a semiconductor structure consisting of a layer of single crystalline silicon separated from the bulk substrate by a thin layer of insulator. Silicon on insulator wafers are still compatible with complementary metaloxidesemiconductor (CMOS) integrated circuit fabrication. In SOI wafers the insulator mostly is a thermal silicon oxide (SiO_2) layer, and the substrate is a silicon wafer. Depending on the type of application, the silicon film thickness can vary from tens of nanometers to tens of micrometers. Likewise, the buried oxide thickness also ranges from tens of nanometers to several micrometers. Combine SOI wafer and lithography techniques, crystalline silicon waveguides of different thicknesses and widths can be fabricated.

Crystalline silicon possesses many good features for integrated photonics. Crystalline silicon has a high refractive index contrast with air or oxide cladding. Refactive index contrast in a waveguide is a measure of refractive difference in refractive index of the core and the cladding. The refractive index contrast (Δ), is typically given by the following equation:

$$\Delta = \frac{n_{core}^2 - n_{cladding}^2}{2n_{core}^2} \tag{1.5}$$

where n_{core} is the refractive index in the core and $n_{cladding}$ is the refractive index of the cladding. The refractive index of crystalline silicon is around 3.48 at the C-band communication wavelength of 1550 nm. The index contrast of crystalline silicon waveguide is as highs as around 46% with air cladding, and around 41% with silica cladding (refractive index of silica is 1.444 at the wavelength of 1550 nm). Such a high refractive index contrast allows for a tight confinement of light in a small dimension. The typical dimension of a single mode crystalline silicon waveguide is around hundreds of nanometers, and a small dimension allows one to implement unique functionalities on a very compact footprint. However, there are also some curse from very high index contrast because it makes the waveguides more sensitive to scattering losses caused by the nanometer-scale roughness of the sidewalls of the waveguide. Even a roughness of a few nanometers can make propagation loss to be on the order of several dB/cm.

Another important feature of crystalline silicon is the high nonlinearity, which makes crystalline silicon particularly suitable for nonlinear optics demonstrations. For comparison, the typical value of the nonlinear refractive index n_2 in highly nonlinear fiber (HNLF) is around $3 \times 10^{-16}\text{cm}^2/\text{W}$. The typical value of n_2 is around $4 \times 10^{-14}\text{cm}^2/\text{W}$, which is 2 orders higher than HNLF [7].

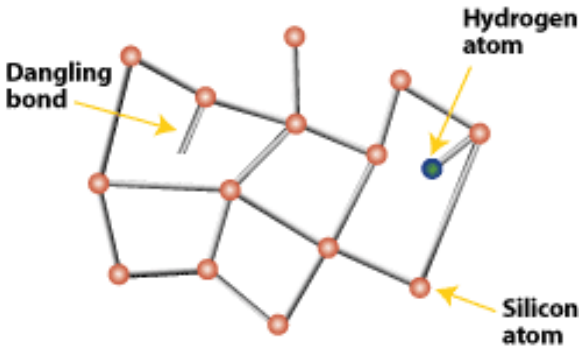

Figure 1.3: Schematic figure of hydrogenated amorphous silicon (from http://www.daviddarling.info/encyclopedia)

1.3.2 Hydrogenated amorphous silicon

Amorphous silicon is the non-crystalline form of silicon. As shown in Figure 1.3, due to the disordered nature, some silicon atoms may have dangling bonds, which can be passivated by hydrogen atoms to form hydrogenated amorphous silicon (a-Si:H). The dangling bonds in amorphous silicon cause high optical loss, and the hydrogen passivation can greatly alleviate the induced optical loss.

A-Si:H has attracted a huge attention from people during the past decade and has been proved to be a highly promising new material for nonlinear photonics due to multiple features. First of all, a-Si:H has a similar refractive index with crystalline silicon, and therefore it has a high refractive index contrast with silica cladding. Similarly, the high refractive index contrast enables a tight confinement and a high light intensity in the waveguides, and allows for dispersion engineering. Secondly, a-Si:H can be deposited using Plasma Enhanced Chemical Vapor Deposition (PECVD) at low temperature (150 $\sim$ 300℃), so it is compatible with back-end CMOS processes

and allows vertical stacking of photonics layers. Finally, the most important feature of a-Si:H is the significantly high 3rd order nonlinearity, which is one magnitude higher than crystalline silicon. Many power efficient nonlinear photonics devices have been proved based on this material [8–10].

1.3.3 Silicon nitride

Silicon nitride (SiN) is a common material in CMOS fabrication techniques and is typically deposited by either Low Pressure Chemical Vapour Deposition (LPCVD) at high temperature (larger than 700 ℃) or by Plasma Enhanced Chemical Vapour Deposition (PECVD) at low temperature (less than 300 ℃). LPCVD-based SiN is typically close to stoichiometric Si_3N_4, is highly strained and provides a very low loss. PECVD-based nitride has a composition that depends strongly on the deposition conditions and can be silicon-rich (higher refractive index) or nitrogen-rich (lower refractive index). Both types of nitride have been used for photonic ICs.

Silicon nitride has a refractive index of around 2.0 at a wavelength of 1550 nm, which means a lower index contrast with oxide cladding. Therefore, silicon nitride photonics circuits will not allow a footprint as compact as SOI platform, but the dimension is still in the order of microns. However, this relatively large dimension brings in one other benefit, which makes the waveguide less prone to scattering losses caused by the sidewall roughness. The optical loss of silicon nitride can be 1 or 2 orders of magnitude less than crystalline silicon, which makes silicon nitride suitable

for high Q factor resonators.

As for the nonlinearity, the nonlinear refractive index of silicon nitride is 1 order of magnitude less than crystalline silicon, which is still a decently large value and 1 order of magnitude larger than HNLF. The nonlinearity in silicon nitride waveguides sits in a nice middle ground with a very low optical loss. This combination of features makes silicon nitride particularly suitable for comb generations in micro-ring resonators.

1.3.4 Conclusion

SOI-based silicon photonics has evolved to being a mature PIC-platform that is used in commercial products. But it is not the only option for high-index-contrast waveguide circuits manufactured in a CMOS compatible platform. Other materials platform such as hydrogenated amorphous silicon and silicon nitride are also emerging as an alternative silicon photonics platform, with complementary features and strengths.

Chapter 2

Phase-sensitive Amplification in a-Si:H Waveguides

2.1 Introduction

Optical communication systems require optical amplifiers to compensate for the propagation loss. Most amplifiers used in current systems are phase insensitive amplifiers (PIAs), such as erbium-doped fiber amplifier (EDFA) and Raman fiber amplifier. Phase-sensitive amplification (PSA) can considerably improve the performance of optical communication systems and allow for advanced signal processing functionalities [11, 12]. PSA can be achieved using the nonlinear optical process of four-wave mixing (FWM). Many demonstrations of PSA rely on highly nonlinear optical fibers (HNLFs) which are large-scale and not integrable, and suffer from Stimulate Bragg

Scattering (SBS) [12]. Combining all-optical processes such as PSA with an integrated optical platform can enable ultrafast optical communication systems with reduced size, weight, power consumption and cost. The first on-chip PSA demonstration based on FWM has been reported using chalcogenide (As_2S_3) ridge waveguide [13]. Other on-chip PSA demonstrations have been reported in other platforms, such as $Ga_{0.5}In_{0.5}P$ photonic crystal waveguides [14] and AlGaAs waveguides [15].

As we mentioned in the previous chapter before, silicon is considered as a promising material for nonlinear integrated optical interactions such as PSA due to its high nonlinearity and compatibility with complementary-metal-oxide-semiconductor (CMOS) fabrication processes, and a PSA demonstration achieving 11-dB phase-sensitive extinction ratio was reported with a 38.6 MHz pulse operation in silicon photonic crystal waveguides [16]. At telecommunication wavelengths, a major drawback of silicon platform is the presence of two-photon absorption (TPA) and the accompanying free carriers (FCs) [17]. A p-i-n junction across the waveguide was incorporated to decrease the FC absorption thereby achieving a 20 dB phase-sensitive extinction ratio with continuous-wave (CW) operation; and 14 dB of receiver sensitivity improvement was shown for phase regeneration of 10 Gb/s DPSK signal [18]. Also, a polarization assisted PSA was demonstrated in a Silicon Germanium (SiGe) waveguide, achieving a phase-sensitive extinction ratio of 29 dB; and 2-dB improvement was achieved for phase regeneration of a 20-Gb/s DPSK signal [19].

2.2 Phase-sensitive amplification

The diagram in Figure 2.1(a) shows the principle of phase-insensitive amplification (PIA). As shown in the diagram, the in-phase and quadrature signal components will experience identical gain in phase-insensitive amplification. As a result the field amplitude will get the same amplification for different input phase and the output phase will keep the same with the input phase. As comparison, there is another type of amplification, which is call phase-sensitive amplification (PSA). The principle is shown in Figure 2.1(b). As shown in the right diagram, the in-phase signal component experience a gain, while the quadrature signal component experience an extinction. Therefore, the output signal will get different amplification (gain or extinction) by changing the input phase. Moreover, the output phase will be aligned more closely towards the in-phase axis shown in this diagram. This effect is called phase squeezing effect, which can be seen more clearly from the figure of phase transfer function. Phase transfer function shows the output phase of the signal as a function of the input phase. Figure 2.1(c) shows the phase transfer function of phase sensitive amplification, presenting a typical S curve with most values separated to two discrete states. The phase squeezing effect and the discrete phase transfer function make PSA inherently suitable for phase regeneration of phase coded signal. Phase regeneration of 40-Gbit/s differential phase shift keying (DPSK) signal has been demonstrated in fibers based on PSA [11]. Another application of PSA is to improve the noise figure during the amplification process. In principle, there is a 3 dB quantum limit of noise figure in

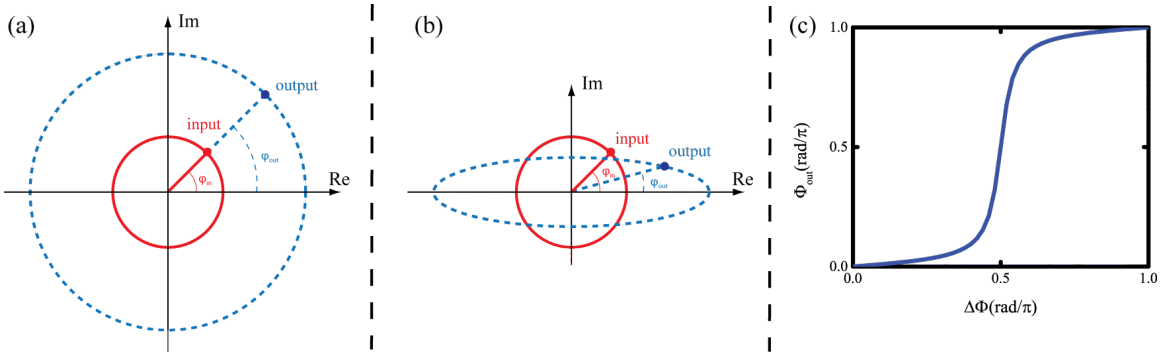

Figure 2.1: (a) The diagram illustrating the principle of phase-insensitive amplification. (b) The diagram illustrating the principle of phase-sensitive amplification. (c) Phase transfer function of the illustrated phase sensitive amplification.

phase insensitive amplification [20]. PSA has the potential to remove this limit and realize noiseless amplification.

2.3 Four wave mixing

Four wave mixing (FWM) is an important third order nonlinear effect, as is described with a $\chi^{(3)}$ coefficient. In a typical FWM, two pumps photons will be transferred to a signal photon and an idler photon. This process is shown in Figure 2.2. As we can see, this parametric process is a energy conservation process, which means that

$$\omega_{pump1} + \omega_{pump2} = \omega_{signal} + \omega_{idler} \ . \tag{2.1}$$

In pump-degenerate FWM, the two pump photons have the same wavelength and thereby energy.

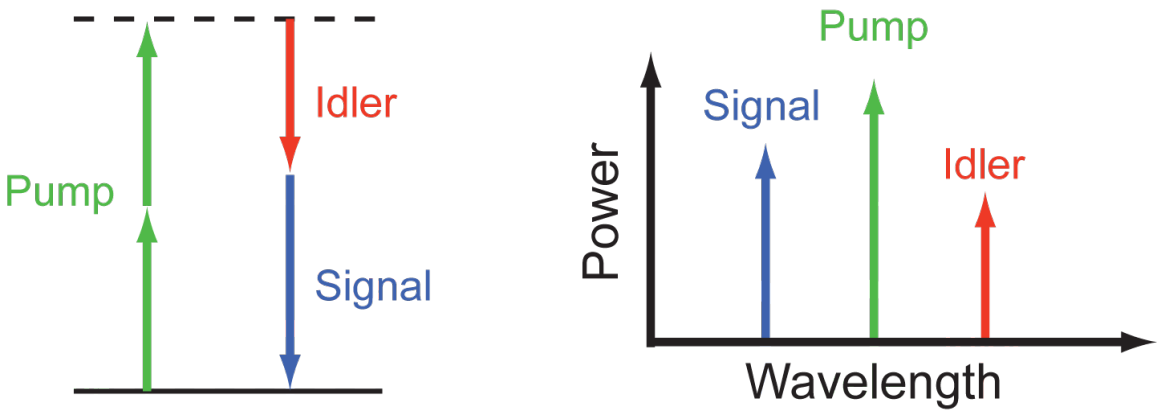

Figure 2.2: Energy diagram of the photons involved in FWM. In pump-degenerate FWM, the two pump photons have the same wavelength and thereby energy.

Moreover, Four wave mixing is a phase-sensitive process, which means the generated signal and idler wave will have a fixed phase relation with the pump wave, so it is inherently suitable for PSA demonstration. There are two main architectures for providing phase-sensitive amplification; signal-degenerate and pump-degenerate. The difference between these two schemes is their degeneracy of the waves. In order to observe the phase-sensitive nature of the gain, all the waves in the FWM interaction must be seeded. As shown in Figure 2.3(a), in the signal-degenerate architecture signal wave and idler wave are degenerate. One degenerate signal/idler wave is centered between two strong pump waves. This degenerate signal/idler wave can get different amplification, gain or extinction, by changing the phase applied onto it. As shown in Figure 2.3(b), in the pump degenerate architecture the two pump waves are degenerate. As shown in this diagram, one strong degenerate pump wave is centered between signal and idler waves. By changing the phase applied to the degenerate pump wave, both signal and idler wave will experience different amplification.

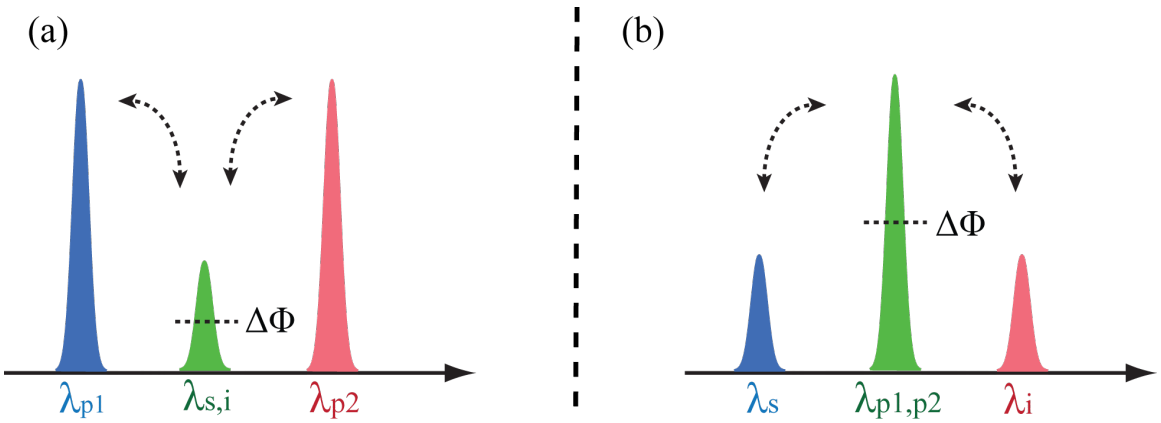

Figure 2.3: (a) The diagram illustrating signal-degenerate four wave mixing for PSA. (b) The diagram illustrating pump-degenerate four waving mixing for PSA using pulse operation.

2.4 Hydrogenated amorphous silicon

Amorphous silicon is the non-crystalline form of silicon. Due to the disordered nature, some silicon atoms will have dangling bonds, which can be passivated by hydrogen atoms to form hydrogenated amorphous silicon (a-Si:H). A-Si:H has attracted a huge attention from people during the past decade and has been proved to be a highly promising new material for nonlinear photonics due to multiple features. First of all, a-Si:H has a similar refractive index with crystalline silicon, and therefore it has a high refractive index contrast with silica cladding. The high refractive index contrast enables a tight confinement and a high light intensity in the waveguides, and allows for dispersion engineering. Also, a-Si:H can be deposited using Plasma Enhanced Chemical Vapor Deposition (PECVD) at low temperature (150 ˜ 300℃), so it is compatible with back-end CMOS processes and allows vertical stacking of photonics layers. The most important feature of a-Si:H is the significantly high 3rd order

nonlinearity, which is one magnitude higher than crystalline silicon. Many power efficient nonlinear photonics devices have been proved based on this material [8–10]. By taking advantage of the high nonlinearity, we successfully demonstrate PSA in a-Si:H waveguides.

2.5 Waveguide design and fabrication

In order to achieve a high efficiency FWM process, the dispersion of the waveguide is carefully engineered by varying the cross section dimension of the waveguide. For this application, we want the dispersion to be anomalous and close to zero at the pump wavelength, which is 1550 nm. Therefore, we chose the dimension to be 500 nm $\times$ 205 nm.

The a-Si:H waveguide is fabricated by using standard microelectronics fabrication techniques in CNSTs NanoFab at NIST. We started from a silicon wafer with 3 μm thermal silicon dioxide layer. After the standard RCA clean, the a-Si:H film is deposited using PECVD on silicon wafer with 3 μm thermal oxidation. The deposition temperature is kept at 300 ℃. Another layer of silicon dioxide is deposited as a hard mask by PECVD to reduce effects from direct etching with organic resists. Then we pattern with JEOL electron-beam lithography and the resist used is MaN-2403. Resist served as a mask when we etched the pattern into the thermal oxide layer via reactive ion etching (RIE). This oxide layer then served as a hard mask for etching

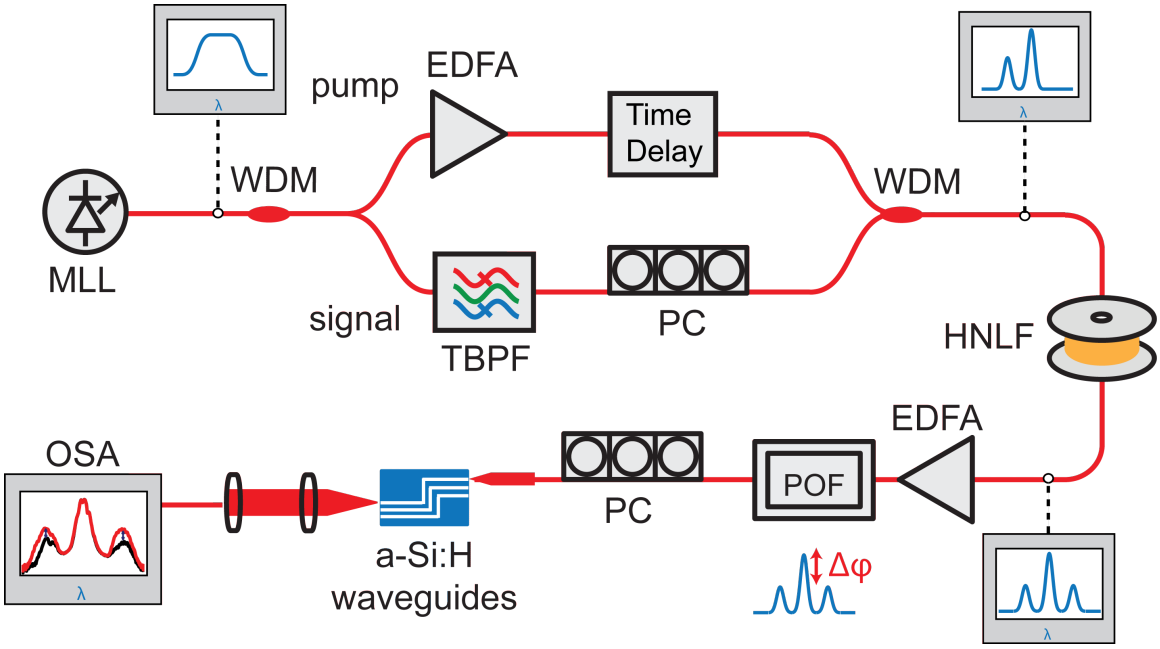

Figure 2.4: Experimental setup for PSA demonstration in hydrogenated amorphous Silicon waveguide.

the pattern into the silicon layer via inductively-coupled plasma (ICP) etching. In the end, we cladded the resulting silicon waveguides with 1 μm of silicon dioxide via PECVD. The input coupling loss for fiber-to-waveguide end is 8.5 dB, with a linear propagation loss of 3.2 dB/cm for TE mode.

2.6 Experimental setup and results

2.6.1 PSA at 90-MHz operation

The experimental setup for PSA demonstration in a-Si:H waveguides is depicted in Figure 2.4. In order to observe the phase-sensitive nature of FWM process, a set

of synchronized pulsed pump, signal and idler waves must be generated in a fixed relative phase relation. The pump and idle waves are generated by filtering from a 90 MHz mode-lock laser (MLL) centered at 1559 nm. The pump pulse is tailored using wavelength-division multiplexer (WDM) at the center wavelength of 1559 nm and pre-amplified by an Erbium-doped fiber amplifier (EDFA). The signal wave is filtered by a tunable band-pass filter (TBPF). A tunable time delay and a polarization controller allow the pulsed pump and the signal to be aligned both in time and polarization. The pump and signal waves are then combined using another WDM and sent together into 35 meters of HNLF to generate the idler wave via FWM process. The generated idler waves are polarized in the same direction, synchronized in time with identical repetition rates and their relative phases are inherently matched. The pump/signal/idler waves are re-amplified by an EDFA to a maximum average power of 26 dBm. A Waveshaper is used to apply a phase shift to the pump wave, compensate the dispersion and filter out the amplified spontaneous emission (ASE) noise introduced from the amplifying process of EDFA. Another polarization controller allows all the waves to be matched to the TE polarization of the a-Si:H waveguide and coupled into the chip via lensed fiber. The exiting light is then collimated by a lens, filtered using a polarizer and then sent into an optical spectrum analyzer (OSA) for measurement.

For analyzing the PSA process, the phase shift is applied only to the pump wave with the POF, while the signal and idler wave phases are unchanged, and the resulting

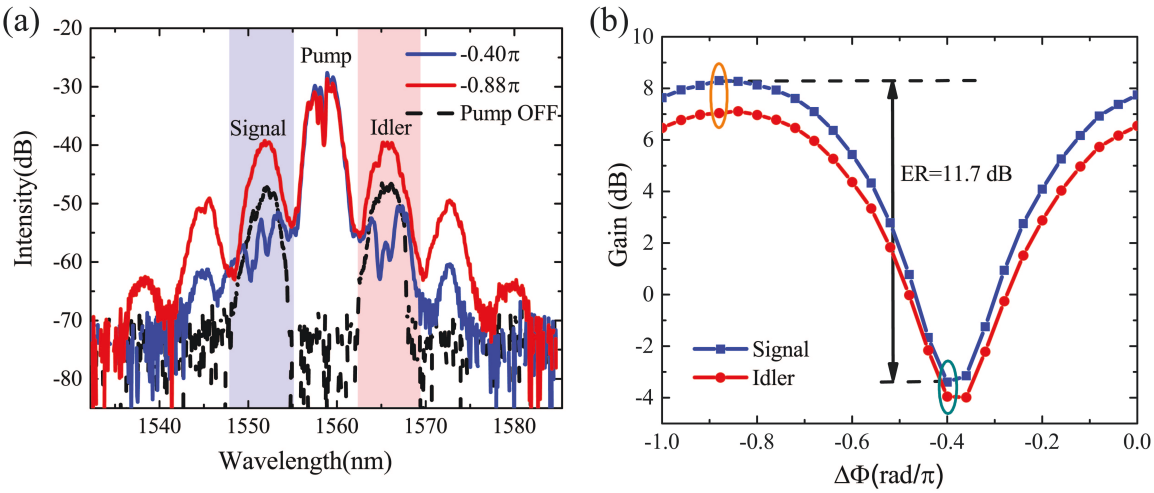

Figure 2.5: (a) The output spectra with different relative phases (solid lines), and output spectra without pump wave (dashed line). (b) Phase-sensitive gain for signal and idler waves as a function of the relative phase of pump wave at a peak power of 1.6 W.

spectra are measured with the OSA. Figure 2.5(a) presents the output signal/idler waves with the pump pulse blocked (dashed line), as well as the output spectra with two different phases applied to the center pump wave (solid lines). The figure clearly demonstrates that the intensity of signal and idler waves varies as a function of applied phase shift. The dip structure of the pump pulse can be attributed to self-phase modulation (SPM) occurred in the a-Si:H waveguide. The ripple structure in the signal and idler wave at $\Delta\Phi = -0.40\pi$, which is the maximum attenuation situation, is caused by the dispersion prior to PSA [21]. However, for the case of maximum gain, the impact of the dispersion is not very significant, due to an S-curved PSA phase transfer function. In order to more clearly show the phase-sensitive nature of the FWM process, we calculate the gain as the ratio of the integral of the signal (idler) power with the pump wave ON over the integral of the signal (idler) power

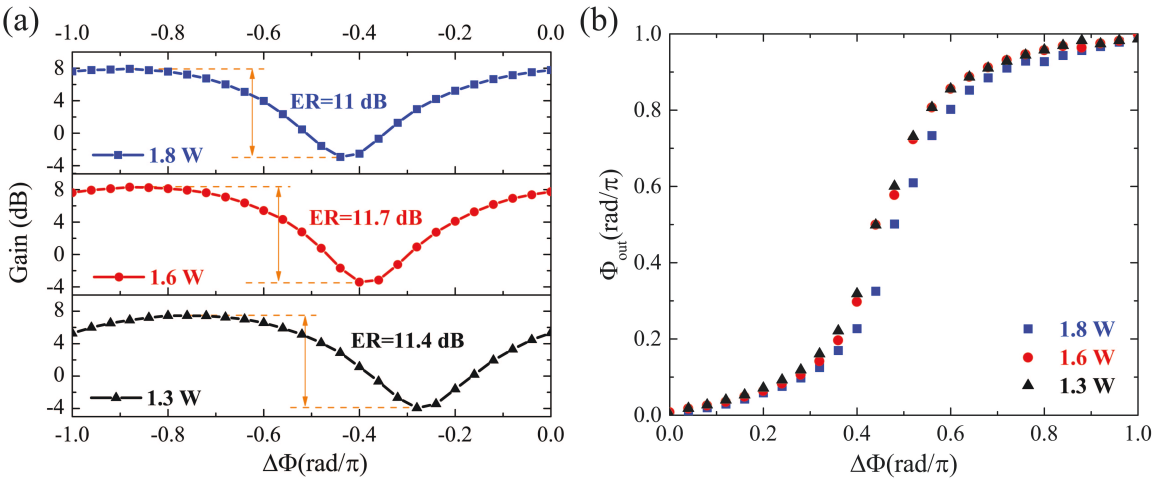

Figure 2.6: (a) Signal gain curves at varying peak pump powers at 90 MHz operation. (b) Phase-transfer function calculated from gain curves at three different peak pump powers.

with the pump wave OFF at the output of the waveguide. The region of integration for the respective waves is highlighted with shading in the spectra of Figure 2.5(a). Figure 2.5(b) summarizes the variation of the PSA gain as a function of the shifted pump phase over one period, which is π for degenerate FWM scheme, for both signal and idler waves. With a peak pump power of 1.6 W, a maximum signal gain of 8.3 dB was obtained at $\Delta\Phi = -0.88\pi$, and a maximum signal attenuation of -3.39 dB was obtained at $\Delta\Phi = -0.40\pi$. As expected,the phase difference between the maximum gain and maximum attenuation position is $\pi/2$. Therefore, we obtained a total extinction ratio (ER) of 11.7 dB. The maximum and minimum gain of idler wave is slightly different from signal wave and the idiler is shown to have an ER of 11.1 dB, because the input peak power and the dispersion are not exactly identical at the signal and idler wavelengths.

We also study the dependence of the PSA gain on the pump power. Figure 2.6(a) summarizes the variation of the PSA gain on the signal as a function of varying phase for three different pump peak powers. The shifting of the phase position of maximum gain and maximum attenuation occurs with varying peak pump power is due to larger pump powers causing larger nonlinear phase shifts. As can be seen in the figure, the phase-sensitive ER does not vary much with increasing pump power. As a result, at an input peak pump power larger than 1.3 W, the phase sensitive ER begins to saturate due to nonlinear loss mechanisms. The phase-transfer function directly provides the relation between the input and output phases, and it determines how well the amplifier can remove phase noise from phase-encoded signals. The phase-transfer function can be calculated from the measured phase-sensitive gain using the method derived in [22]:

$$tan^2\phi_{out} = \left(\frac{G_{min}}{G_{max}}\right) \cdot \left(\frac{G - G_{max}}{G_{min} - G}\right) \ . \tag{2.2}$$

Figure 2.6(b) shows the PSA phase-transfer function for the 3 different pump powers. As seen in the figure, most values of input phase and output phase are separated to values close to two discrete states, and clearly present a typical S-curved phase transfer function. However, the calculated phase transfer function looks similar for 3 different input peak pump power, because the ER has already saturated at this power level.

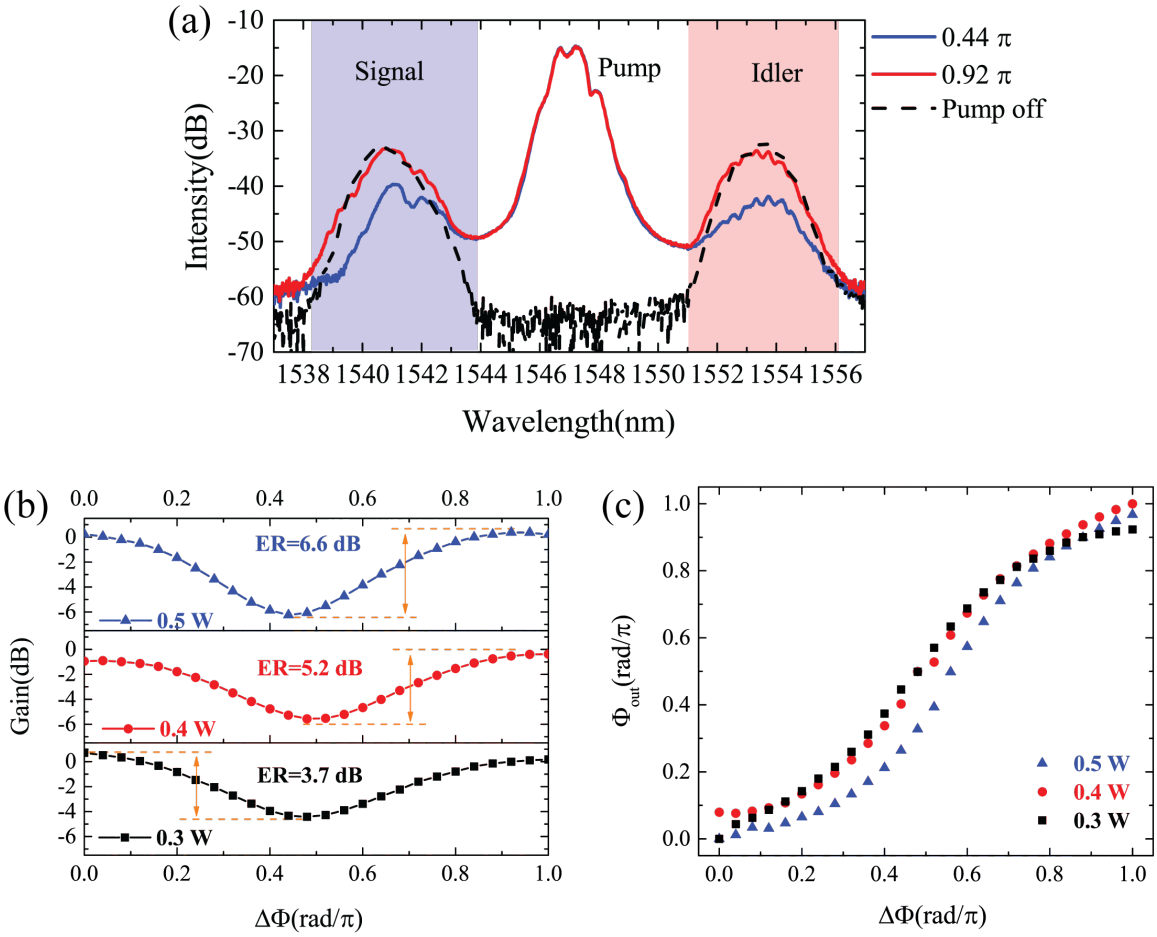

Figure 2.7: Phase sensitive amplification at 10-GHz operation. (a) Output spectra without pump wave (dashed line), and with different relative phases (solid lines). (b) Signal gain curves at varying pump powers. (c) Phase-transfer function calculated from different gain curves at three different powers.

2.6.2 PSA at 10-GHz operation

The output spectra with different relative phases (solid lines) and without pump wave (dashed line) under 10-GHz pulse operation are presented in Figure 2.7(a). The figure clearly shows the variation in the intensities of signal and idler waves by changing the applied phase to the pump wave. Although phase sensitive extinction is clearly achieved, the maximum gain in the high repetition rate case is reduced

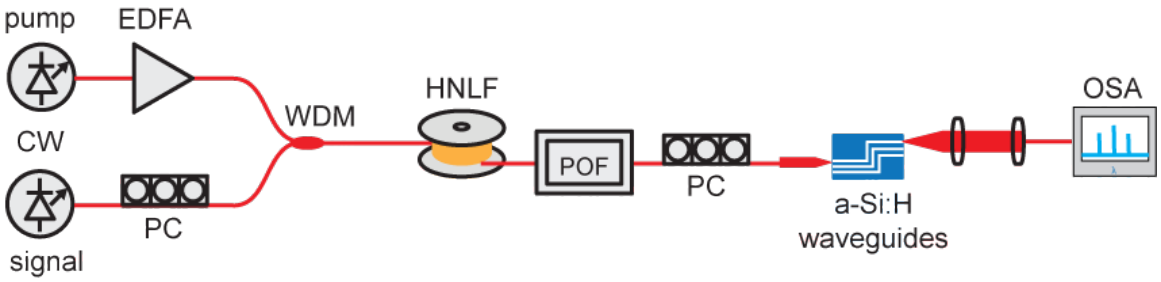

Figure 2.8: Experimental setup of PSA demonstration using continuous-wave light.

due to the presence of nonlinear loss mechanisms as compared to the 90 MHz pulse operation. The intensities of signal and idler shown in the output spectrum are very similar at maximum gain ($\Delta\Phi = -0.92\pi$) as they are with the pump wave OFF, indicating minimal gain. Figure 2.7(b) presents the signal gain curves as a function of relative phase for 3 peak pump powers. Notably, we can still achieve an ER of 6.6 (7.9) dB for the signal (idler) wave at a pump power of 0.5 W at a high-repetition rate of 10-GHz. Moreover, when increasing the peak power from 0.3 W to 0.5 W, the ER continues to increase from 3.7 dB to 6.6 dB, indicating the PSA process is not yet saturated due to nonlinear loss mechanisms. This indicates the potential for increased performance with higher peak pump powers. Figure 2.7(c) shows the phase transfer function calculated from the signal gain curve for two different pump powers at 10-GHz operation. The phase transfer function is less defined than that under 90-MHz pulse operation due to a lower ER.

2.6.3 PSA using continuous-wave Light

In order to further study the FCA effect on PSA in a-Si:H waveguides, we also carry out the PSA experiment using continuous-wave (CW) light. Figure 2.8 shows the experimental setup of PSA demonstration using continuous-wave light. This experiment is performed using two CW lasers. The pump wave is centered at 1558 nm and amplified to 0.5 W using an EDFA. The signal wave is centered at 1554 nm, combined with the pump wave and sent into 100 meters of HNLF to generate the idler wave via FWM. All three waves are then sent into the programmable optical spectral filter to apply a phase shift on the pump wave. The signal is attenuated to match the signal and idler wave intensity. After that, the same experimental setup as in Fig.1 is used to investigate the phase sensitive behavior. Figure 2.9(a) presents the output spectra in linear scale with two different phase shifts, and the spectrum with the pump wave off (black curve). The power coupled into the device is 38 mW. The figure shows variation in the intensities of both signal and idler waves with different applied phase shift on pump wave. As compared with the pulsed operation, the phase sensitive operation is less significant in the CW operation since both the signal and the idler wave suffer higher losses with the presence of the pump wave. At the phase that produces the maximum gain ($\Delta\Phi = 0.85\pi$), the signal experiences 5.9 dB loss with the pump on. Figure 2.9(b) presents the signal gain curves at two different pump power. With increasing the power from 21 mW to 38 mW, the phase-sensitive ER increases from 0.7 dB to 1.6 dB, but the maximum gain decreases from -4.3 dB to

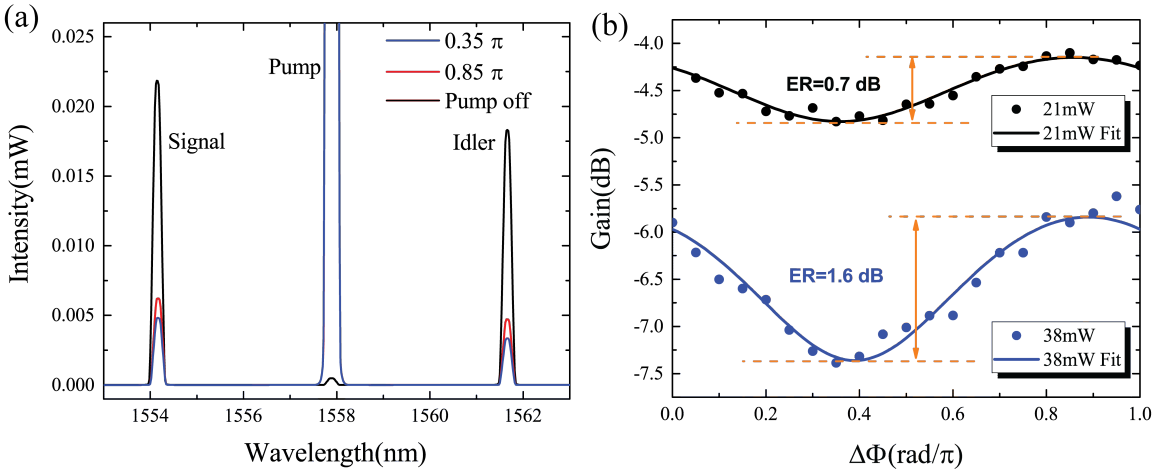

Figure 2.9: Phase sensitive amplification demonstration using continuous-wave light with an input power of 38 mW. (a) Output spectra with different relative phases, compared with the spectrum with the pump wave off. (b) Signal gain curves at two varying pump powers.

-5.9 dB due to a higher nonlinear loss. The phase-sensitive ER is expected to increase with higher pump powers.

2.7 Conclusion

In summary, we experimentally demonstrate phase-sensitive amplification based on pump-degenerate FWM in a-Si:H waveguides under 90-MHz and 10-GHz pulsed operation. At 90 MHz, a maximum extinction ratio of 11.7 dB is achieved with 1.6 W peak pump power. Due to the high nonlinearity and nonlinear figure of merit in a-Si:H, we are able to achieve a 6.6 dB extinction ratio at 0.5 W peak pump power at 10 GHz. This is obtained at this communication data rate without any attempt to mitigate the effects of nonlinear loss mechanisms (such as a p-i-n diode

structure for carrier removal). We also demonstrate phase-sensitive operation in this waveguide at continuous-wave operation of 1.6 dB ER with an input power of 38 mW. This platform is backend compatible with CMOS fabrication processing and has the potential to enable on-chip all-optical phase and amplitude regeneration.

Chapter 3

Mid-IR Supercontinuum Generation in a-Si:H Waveguides

3.1 Introduction

Broadband supercontinuum generation (SCG) is of great interest for applications such as spectroscopy, optical coherence tomography, and wavelength division multiplexing in telecommunications. In photonic crystal fibers [23], an increased effective nonlinearity and the ability to tailor dispersion with high precision has enabled large bandwidth SCG spectra. On-chip integrated supercontinuum sources based on compact devices has the potential of providing integrated components with small footprints that can be fabricated at low costs.

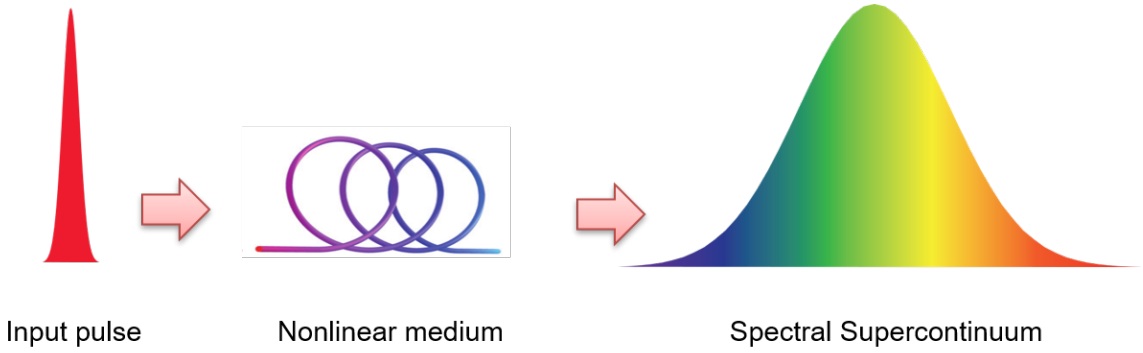

Figure 3.1: Supercontinuum generation takes place when a strong short pulse is incident into nonlinear mediums.

3.2 Supercontinuum generation

When a strong narrow-band pulse is incident into nonlinear medium, a spectral broadening will happen and generate a broadband spectrally continuous output as shown in Figure 3.1. This phenomenon is called supercontinuum generation. Light sources based on supercontinuum can provide a combination of desirable features, such as high output power, broad bandwidth, and high degree of coherence. These features make supercontinuum ideal for many applications, such as optical frequency comb technologies, light sources for optical coherence tomography (OCT) imaging system and broad bandwidth spectroscopy, especially for molecule sensing in the mid-IR wavelength range. The most common vibrational resonances in organic molecules are in the mid-infrared wavelength range. Unfortunately, the supercontinuum in conventional glass fibers is limited to visible and near-infrared wavelengths up to 2 micrometer. Guided-wave supercontinuum generation was originally observed using Ti:Sapphire laser pulses in photonic crystal fibers due to their enhanced nonlinearity

and the ability to tailor the fibers dispersion [23]. More recently, on-chip integrated supercontinuum sources have been of interest due to their extremely compact size, low cost, tailorable dispersion, and often larger nonlinearity. Specifically, on-chip SCG has been demonstrated in chalcogenide [24], silicon nitride [25], lithium niobate [26], and both crystalline and amorphous silicon [27, 28]waveguides. Relative to other platforms, the silicon-on-insulator (SOI) platform possesses both high refractive index contrast and high nonlinearities. However, the generation bandwidth in crystalline silicon has been limited by large two-photon absorption (TPA) at telecom wavelengths. However, by working at longer wavelengths TPA is suppressed. Recently, hydrogenated amorphous silicon (a-Si:H) has been found to possess an even higher nonlinearity [10] and a higher bandgap than crystalline silicon. Therefore, the use of hydrogenated amorphous silicon waveguides and a longer wavelength thulium-doped fiber (TDF) laser source is a promising approach for SCG in the mid-IR range [28].

Recently [28], telecom to mid-IR spanning SCG was measured in a-Si:H. However, the picosecond-length pump pulses utilized in this experiment generate supercontinuum that is primarily characterized by four-wave mixing and modulation instability bands generated from noise [23]; and therefore the spectrum lacks coherence limiting its application for optical frequency comb technologies. Using a shorter femtosecond pulsed pump source will yield a different SCG regime in which self-phase modulation (SPM) and soliton fission are dominant yielding high coherence. Here, using a 160-fs pulsed pump Thulium-doped fiber laser centered at 1910 nm we demonstrate coher-

ent SCG spanning from 1.63 μm to 2.42 μm in a hydrogenated amorphous silicon waveguide.

3.3 Waveguide design and fabrication

In order to achieve broadband supercontinuum, the group velocity dispersion at pump wavelength is required to be anomalous and close to zero. As we mentioned before, the high index contrast allows for dispersion engineering of the waveguides. We carefully design the geometry of our a-Si:H waveguide and the cross section of the fabricated channel waveguide is 330 nm tall by 900 nm wide with a waveguide length of 6 mm. The group velocity dispersion (GVD) of the fundamental TE mode is calculated using a commercial mode solver (FimmWave) and shown in Figure 3.2(a). The engineered waveguide exhibits anomalous dispersion (D = 174 ps/nm $\cdot$ km). Therefore this geometry gives us anomalous group velocity dispersion at the pump wavelength of 1910 nm, which is the typical wavelength of Thulium-doped fiber laser. Figure 3.2(b) shows the calculated TE mode profile.

As mentioned before, our a-Si:H waveguide is fabricated using standard CMOS manufacturing techniques. We started from a silicon wafer with 3 μm thermal silicon dioxide layer and the a-Si:H film is deposited using plasma enhanced chemical vapor deposition (PECVD). The fabrication process is similar with the previously mentioned method. We measure the propagation loss of the waveguide to be 10 dB/cm in TE-

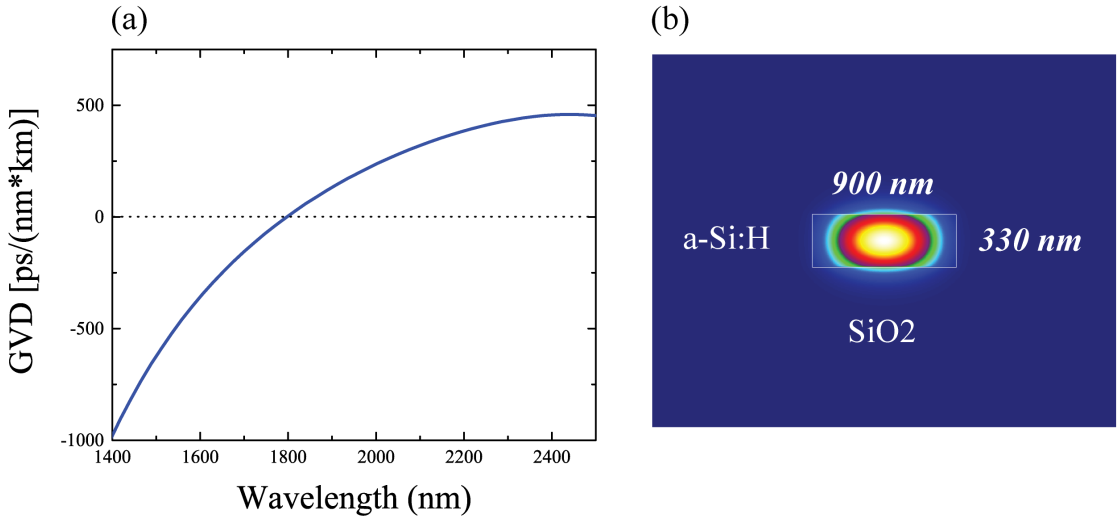

Figure 3.2: (a) Group velocity dispersion of the a-Si:H waveguide as a function of the wavelength. (b) Plot of calculated TE mode profile.

mode at the mid-IR wavelength of 1910 nm.

3.4 Experimental setup and results

The pump laser is an all-fiber femtosecond source based on a mode-locked fiber laser at 1550 nm that is Raman-shifted into the amplification band of a Thulium-doped fiber amplifier. The laser has a repetition rate of 50 MHz and its center wavelength is tunable between 1850 nm and 1950 nm. The center wavelength of the laser is tuned to 1910 nm, which is close to the zero-dispersion wavelength in the anomalous region of the waveguide. As shown in Figure 3.3, the pump pulse is sent through a polarization rotator and a polarizer to ensure coupling to the fundamental TE mode. Then the pulse is sent into our a-Si:H waveguides and the output is

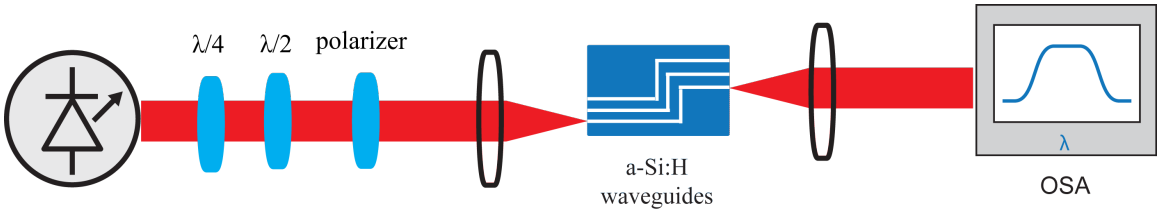

Figure 3.3: Experimental setup for supercontinuum generation in a-Si:H waveguides.

collected using an OSA.

The pump pulse width can be adjusted by controlling the dispersion and nonlinearity in the laser and is initially set to 424 fs. Figure 3.4(a) illustrates the evolution of the output spectrum as the input peak power increases. at a low input power, the pump spectrum is broadened by SPM. When the peak power reaches 27 W, two Modulation Instability (MI) sidebands start to appear due to the parametric amplification of background noise. With increasing power, these two MI sidebands merge with the SPM broadened spectrum, and form a broadband supercontinuum. However, this continuum lacks coherence. In comparison, when the width of the input pump pulse is tuned to 160 fs, the supercontinuum generation spectra exhibit different features. As shown in Figure 3.4(b), the pump spectrum is broadened by self-phase modulation (SPM) at a low input power. As the pump power increases, the spectral width keeps increasing and finally generate a 790nm wide coherent supercontinuum, spanning from 1.63 μm to 2.42 μm, at the highest peak power of 240 W due to SPM and soliton fission resulting in a coherent continuum [23].

We also carry out the nonlinear loss measurement in the hydrogenated amorphous

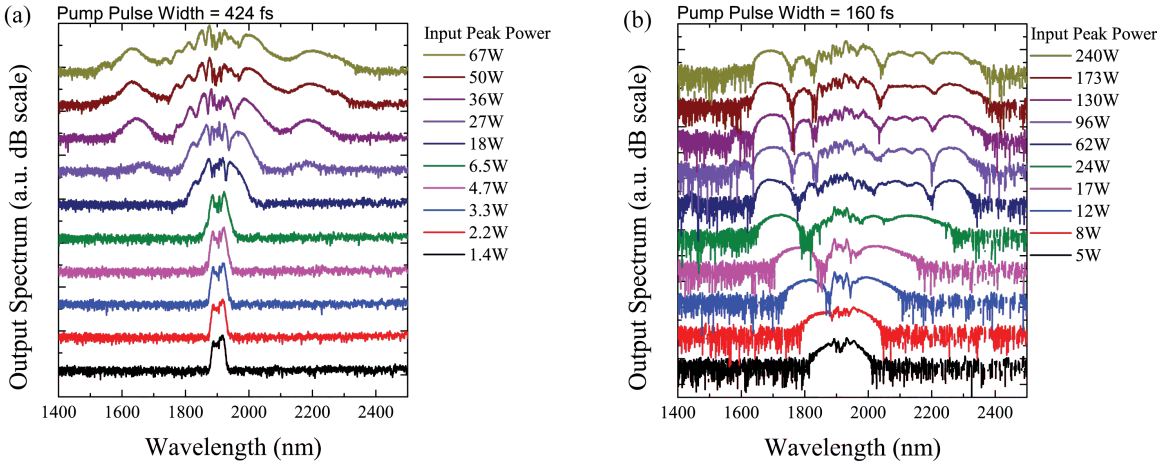

Figure 3.4: Measured output spectra with increasing input peak power at different pulse duration: (a) pulse duration is 424 fs; (b) pulse duration is 160 fs.

silicon waveguides at 1910 nm wavelength. We measured the inverse transmission through the a-Si:H waveguide as a function of input peak pump power, and the results are presented in Figure 3.5. Based on this, we can estimate the imaginary component of the effective nonlinearity Im(γ) using the following equation:

$$\frac{1}{T} = \frac{P_{in}}{P_{out}} = exp(\alpha L) \cdot \frac{L_{eff}}{A_{eff}} \cdot Im(\gamma) \cdot P_{in} + exp(\alpha L) \ , \tag{3.1}$$

where T is the optical transmission, L_{eff} is the effective propagation length and A_{eff} is the effective area. Based on this equation, Im(γ) is calculated to be 6.6 $W^{-1}m^{-1}$ with an effective area of 0.3 μm^2.

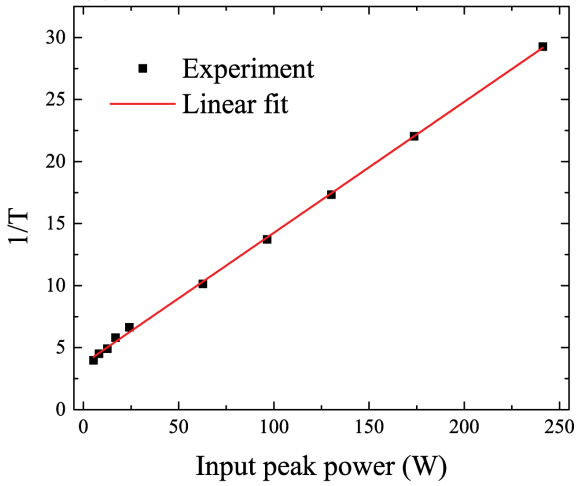

Figure 3.5: The inverse transmission through the a-Si:H waveguide as a function of input peak pump power and the linear fit.

3.5 Conclusion

We successfully demonstrate a 790 nm wide Mid-IR supercontinuum generation, spanning from 1.63 μm to 2.42 μm, using a femtosecond pulsed pump Thulium-dosed fiber laser centered at 1910 nm in a hydrogenated amorphous silicon waveguide.

Table 3.1 illustrates a comparison of on-chip supercontinuum generation found in literature. Among these works, three of them ([28], [31] and our work) are in Mid-IR wavelength range. In this work [28] they are using a picosecond pulse and the generated supercontinuum lacks coherence. The recent work in silicon wire waveguide [31] presents an octave spanning coherent supercontinuum in Mid-IR wavelength range. However, it is required to be pumped at longer wavelength of 2290 nm and requires a more expensive light source. The light source used in this work is a homemade Mid-IR optical parametric oscillator (OPO). In our work, we generate a broadband coherent

Table 3.1: Comparison of on-chip supercontinuum generation in literature.

Material platform	Band-width (nm)	Pulse width (fs)	Pump wave-length (nm)	Frequency (MHz)	Pulse energy (pJ)
Chalcogenide waveguide [24]	760	610	1550	10	60
Si_3N_4 waveguide [25]	1360	200	1300	80	160
a-Si:H waveguide [29]	500	180	1575	82	5
a-Si:H waveguide [30]	550	1600	1530	10	6.4
a-Si:H waveguide [28]	1000	1240	1950	26	21
a-Si:H waveguide [31]	1660	70	2290	100	16
Our a-Si:H waveguide	790	160	1910	50	95

Mid-IR supercontinuum pumped at the typical wavelength of Thulium-based fiber laser.

Chapter 4

Silicon Nitride Micro-ring Resonator for Optical Frequency Comb Generation

4.1 Introduction

Optical frequency comb is an optical spectrum which consists of periodic discrete spectral lines with equidistant spacing. Optical frequency combs can be used as an optical ruler for high-precision frequency metrology [32]. Moreover, optical frequency combs have widespread applications such as spectroscopy [33], broadband gas sensing [34], attosecond pulse generation and many other applications. These applications are all taking advantage of the broad band width and precisely controlled frequency

positions of optical frequency combs. Most applications of optical frequency combs are based on mode-locked lasers, and repetition rates are blew 1 GHz in most cases due to the large dimension of mode-locked laser resonators. For some applications, it would have more benefits to decrease the footprint and increase the repetition rate to above 10 GHz.

Recently, a novel approach based on nonlinear Kerr effect and parametric frequency conversion in microresonators has emerged, and it can provide higher repetition rates above 10 GHz with an ultra-compact footprint. In order to generate optical frequency combs in microresonator, a combination of high Q factor and high nonlinearity is required. A large variety of materials, such as silica [35], silicon nitride [36], calcium fluoride (CaF_2) [37] and magnesium fluoride (MgF_2) [38], are used to fabricate high-Q microresonator.

Silicon nitride is very attractive based on multiple reasons. It is transparent optically over the visible and infrared spectral range. Also, silicon nitride exhibits a high third-order nonlinearity of $n_2 = 2.5 \times 10^{-15}$ cm^2/Watt, which is approximately one order of magnitude larger than that of silica or CaF_2 or MgF_2, but it is 50 times smaller than that of silicon. However, silicon nitride exhibits losses that are at least ten times smaller than that of silicon. Another main benefit of silicon nitride is that it is fully compatible with planar integration and mature microelectronic fabrication technology. Nitride also has the advantage of dispersion engineering to provide a broadband spectrum.

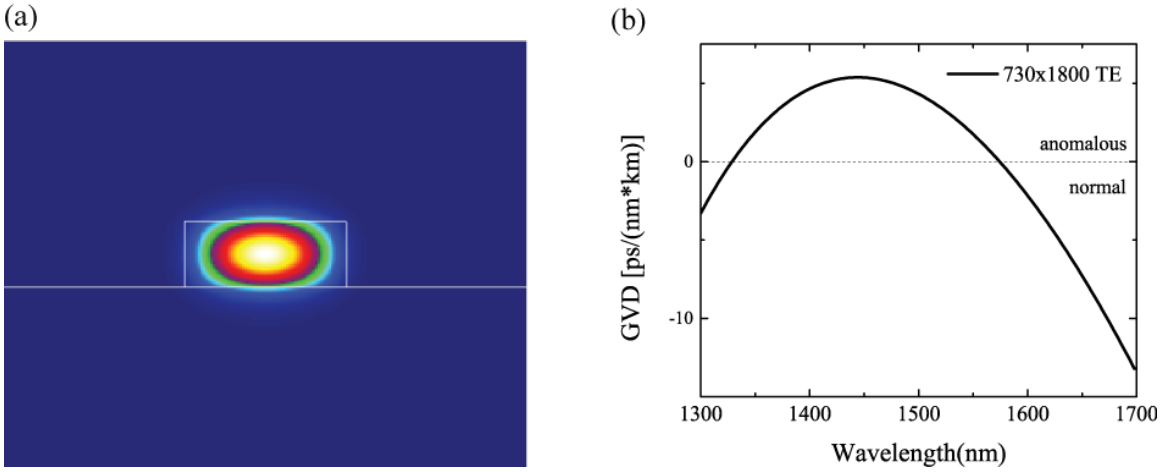

Figure 4.1: (a) Plot of calculated TE mode profile for designed waveguide dimension (730 nm × 1800 nm). (b) Calculated group velocity dispersion (GVD) of nitride waveguide as a function of the wavelength.

4.2 Device design and fabrication

We carefully designed the dimension of the waveguide to be 730 nm high and 1800 nm wide. Figure 4.1(a) shows the calculated fundamental TE mode profile with an incident light at 1550 nm. Figure 4.1(b) exhibits the calculated group velocity dispersion (GVD) of the designed silicon nitride waveguide as a function of wavelength for fundamental TE mode, and the dimension will have anomalous dispersion around 1550 nm.

We fabricated silicon nitride ring resonators by using standard microelectronics fabrication techniques in CNSTs NanoFab at NIST. The fabrication process flow chart is depicted in Figure 4.2. We started from a silicon wafer with 3 μm thermal silicon dioxide layer. After the standard RCA clean, a 730-nm thick silicon nitride layer was then deposited on the top by using low pressure chemical vapor deposition

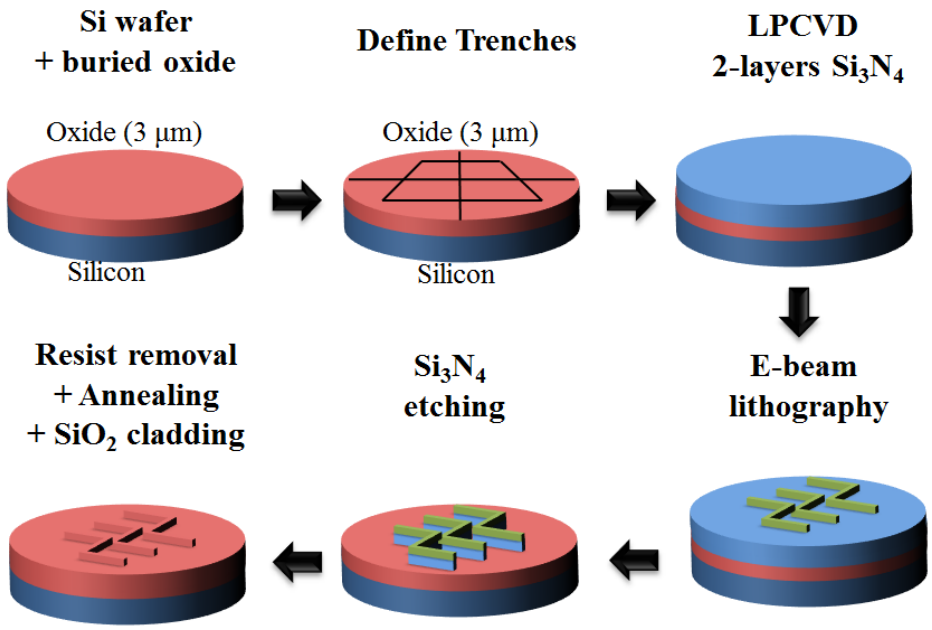

Figure 4.2: Silicon nitride waveguide fabrication processes.

(LPCVD) from dichlorsilane (SiH_2C_{l2}) and ammonia (NH_3). It is known that nitride film exhibits high stress and will easily introduce cracks. In order to avoid the high stress and induced cracks, the deposition is carried out at two steps, allowing wafers cooling down to room temperature in between [39]. Handling the wafers during the fabrication process will induce physical shocks from the edge of the wafer, and this can provide enough energy to crack the film [40]. Once initiated, the cracks will continue propagating until they encounter some resistance. In order to avoid cracks, we use diamond scribe defining trenches to protect photonic devices from cracks. Then we pattern the nitride layer with electron-beam lithography and the resist used is MaN-2405. In order to reduce the sidewall roughness, we use a post bake process for 5 minutes at 115℃ to reflow the resist surface. The wafer was then etched through

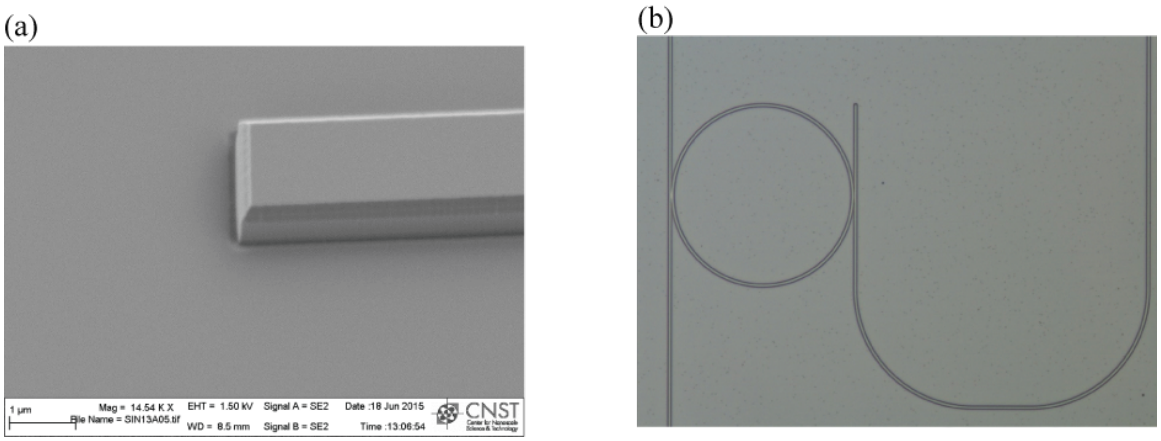

Figure 4.3: (a) Scanning electron microscope (SEM) image of the bus waveguide. (b) SEM image of the microresonator with a drop end.

using reactive ion etching (RIE) with a CHF_3/O_2 chemistry. The etching parameters have been carefully optimized to achieve smooth sidewall with low roughness. After the MaN-2405 resist was removed in an oxygen plasma, the wafer was annealed at 1,100℃ in an ambient nitrogen environment for 2 hours to break the N-H bonds. Annealed devices were then cladded with 1 μm oxide layer using a low temperature oxide furnace.

The SEM image of the bus waveguide is shown in Figure 4.3(a). We can see the waveguide has a very smooth side wall, which can ensure a minimal loss. The SEM image of the ring resonator with a drop end is shown in Figure 4.3(b). The light coupled in the the drop end can also be collected using this design.

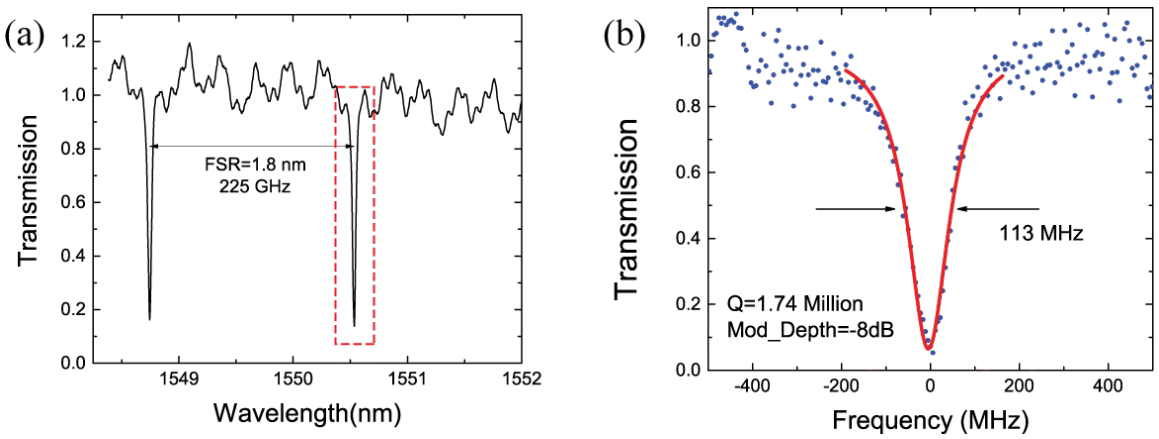

Figure 4.4: (a) Transmission spectrum of silicon nitride micro-ring resonator measured using a broadband light source and OSA. (b) Zoom-in transmission spectrum of a resonance with 113 MHz linewidth corresponding to an intrinsic Q of 1.74 Million.

4.3 Experimental results

We measured the transmission spectrum of the fabricated device in order to measure the Q factor of the ring resonator. Figure 4.4(a) presents the transmission spectrum of silicon nitride micro-ring resonator measured using a broadband light source and OSA. The light couples into the ring resonator at resonances and shows a dip structure in the spectrum. The free spectral range is determined by the resonator size, which is 100 mum, and the FSR for fundamental TE mode is measured to be 225 GHz , which is 1.8 nm at the wavelength of 1550 nm. However, the linewidth of the resonance measured using this method is limited by the OSA resolution and is not correct. In order to correctly calibrate the linewidth, a tunable velocity laser light source is coupled into the bus waveguide, through a polarization controller, a lensed fiber and the inverse nanotaper. We control the polarization to be TE mode, and the coupling loss of TE mode is estimated to be around 7 dB. The output light of

the ring resonator is collected on a photodetector. The laser frequency is finely tuned by applying a triangular wave voltage to the piezoelectric transducer. The result is shown in Figure 4.4(b). The full width at half maximum (FWHM) of the resonance spectrum is measured to be 113 MHz, corresponding to a loaded Q factor of 1.74 million. Based on the measured Q factor, we can calculate propagation loss using this equation:

$$\alpha = \frac{2\pi n_g}{Q \cdot \lambda_0} = \frac{\lambda_0}{Q \cdot R \cdot FSR} \ , \tag{4.1}$$

where n_g is the group index, λ_0 is the resonant wavelength, R is the radius of the ring resonator, and FSR is the free spectral range. The propagation loss is calculated to be 0.11 dB/cm. The gap between the bus waveguide and the ring resonator is designed to be 300 nm, and achieved a nearly critical coupling with a modulation depth of 8 dB.

In order to generate optical frequency combs, we amplify a tunable velocity laser light source with a 2 Watt erbium-doped fiber amplifier (EDFA) and inject it into the bus waveguide using lensed fiber. The polarization is controlled to be quasi-TE mode by using a polarization controller. A WDM centered at 1550 nm is used to filter the amplified spontaneous emission (ASE) noise. The output is collected using an optical spectrum analyzer (OSA). The pump wavelength is started from the shorter wavelength of the resonance, and tuned slowly into resonance. We carefully tuned the

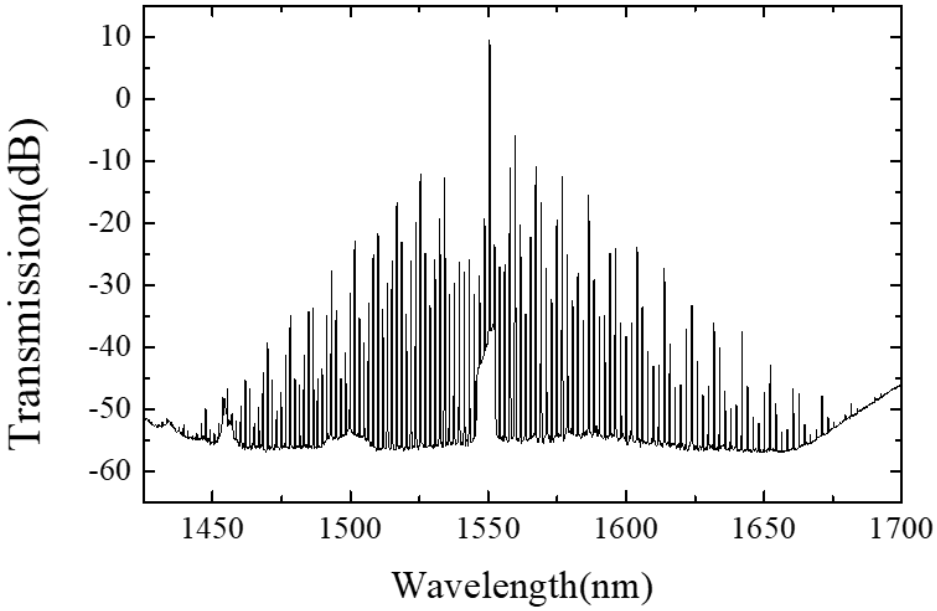

Figure 4.5: Generated Kerr frequency combs from silicon nitride microring.

laser into the resonance from the short wavelength. The resonance is shifted to longer wavelength due to Kerr effect and thermal effect. By slowly tuning the laser into resonance, and when the coupled power exceeds the threshold power, the parametric gain exceeds the one-trip loss, a parametric amplification occurs and optical frequency combs over a bandwidth of more than 240 nm (30 THz) is achieved as shown in Figure 4.5. Bandwidth is limited by the dispersion and the power limitation coupled into the ring resonator. The pump wave is at 1551.3 nm, and the comb spans from 1440nm to 1680 nm. We believed the bandwidth is limited by the input power and dispersion. With a larger input power and better designed dispersion, we hope to get octave spanning frequency combs in the future.

4.4 Conclusion

In summary, we successfully fabricated silicon nitride micro-ring resonators with a Q factor as high as 1.74 million. The propagation loss achieves as low as 0.11 dB/cm. By tuning a continuous wave laser into the resonance of the micro-ring resonator, a parametric amplification occurs and optical frequency combs over a bandwidth of more than 240 nm is achieved.

Chapter 5

Photonic Physical Unclonable Functions using Silicon Nitride Spiral Waveguides

5.1 Introduction

A report from last years Frontier Economics indicates that the global economic value of counterfeiting and piracy could reach US $2.3 trillion by 2022 [1]. Counterfeit integrated circuits (ICs) have become an alarming issue over the past few years as they pose a potential threat to the security and reliability of all kinds of electronic systems [41]. Historically, the major anticounterfeit is to tag each IC chip with a

[1] "The Economic Impacts of Counterfeiting and Piracy: Report prepared for BASCAP and INTA," in Frontier Economics (2016), p. 61.

unique part number and to print a unique serial number on the device package. While this is a low cost and scalable solution, it is extremely vulnerable to IC counterfeiting efforts where, for example, old or defective devices are recycled, or compromised devices are injected into the supply chain. This rise in counterfeit ICs has fueled much research to develop tagging technologies that are unclonable, reliable, easy to authenticate, and inexpensive. Another tactic against electronic cloning is based on tagging chips using clone-proof materials, such as plant DNA [2] from Applied DNA Sciences. However, these plant DNAs can only be identified by shipping back to the lab, thus it is very expensive ($250 per test) and time-consuming for authentication. One recent promising anti-counterfeiting development is to tag electronic circuits using a physical unclonable function (PUF).

5.2 Physical Unclonable Function

Physical unclonable fuctions (PUFs) are physical devices that have an unpredictable yet repeatable transfer function. As shown in Figure 5.1, a PUF works first as a function, which provides a specific response to a specific challenge. Also, PUF is a physical entity,not an algorithm, which means the unique information is stored within the physical structures of the device.PUFs are designed to amplify physical device idiosyncrasies making them difficult to clone.

PUFs have been demonstrated using both electronic and optical technologies.

[2]"DNA Authentication Marking - FSC 5962," (2012).

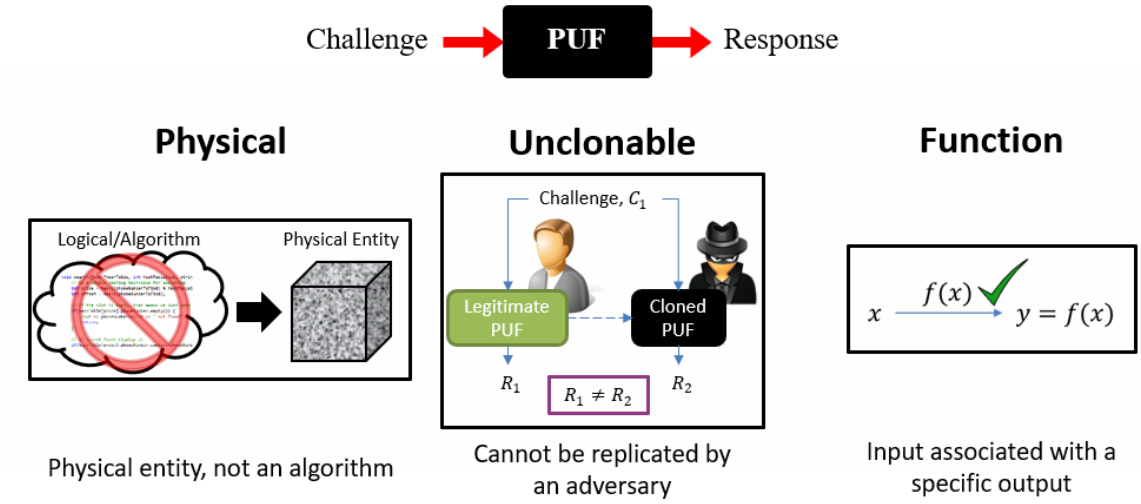

Figure 5.1: Important properties of Physical Unclonable Functions.

While much of the past research has been focused on electronic PUFs, it has been shown that optical PUFs offer more security against cloning attacks and are more difficult to model [42]. The first optical PUF was proposed by Pappu et al. and based on randomly distributed spatial optical scattering [43]. However, most existing optical PUFs are implemented with bulk optical materials and based on camera-based detection and as a result are very sensitive to alignment and not easy to integrate with electronic circuits [44–46]. Recently, our group demonstrated integrated photonic PUFs based on chaotic silicon micro-cavities [47].

5.3 Device Design and Fabrication

PUFs exploit idiosyncrasies in the manufacturing process to produce devices with a uniquely distinct fingerprint. In order to provide an attractive solution to IC coun-

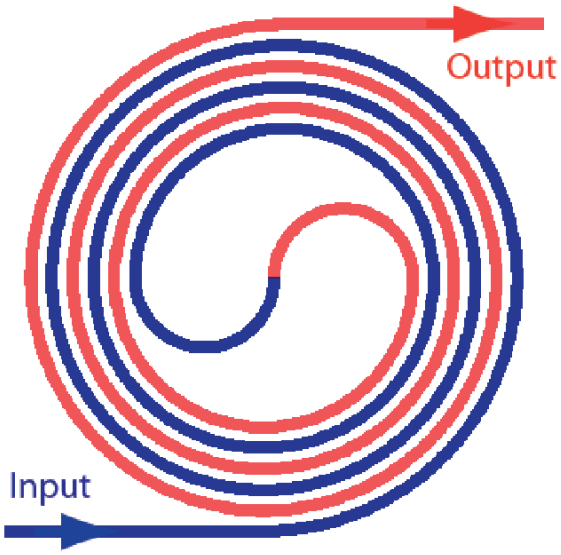

Figure 5.2: Schematic showing architecture of the spiral waveguide.

terfeiting, PUFs should meet the following criteria:

(1) be mass producible and low cost to manufacture,

(2) be compatible with standard CMOS processing,

(3) be extremely robust and repeatable,

(4) be uniquely different in its response from identical copies (i.e. clones).

Here discusses the rationale behind the design of our silicon nitride photonic PUF devices. Inspired by the silicon based spiral spectrometer [48], our spiral PUF takes advantage of the rich spectral response afforded by the interference of different modes in a long, multimode spiral waveguide in order to produce a complex, wavelength dependent intensity response. Figure 5.2 shows a representative diagram of our device design. The device utilizes single mode input and output waveguides in order

to guarantee repeatable excitation of the modes supported by the multimode cavity. Having a rich spectral response is an important design requirement for our application where the complexity of the spectral features is a function of the random delays and path differences between the many supported modes. The low propagation loss in the silicon nitride waveguide allows us to design a large effective cavity and significantly increases the photon interaction between the many waveguide modes. The gap between the adjacent waveguides in the spiral is designed to be small enough to introduce evanescent coupling between counter propagating loops of the spiral. This is better understood when studying the graphic in Figure 5.2: light traveling (primarily) inward in the spiral is highlighted as a red waveguide, whereas light traveling outward is highlighted in blue. Through this interplay of counterpropagating light through evanescent coupling, the effective propagation length for a given photon can vary significantly given the complexity of its path through the device. This provides a more complex frequency response.

The devices are fabricated using standard microelectronics fabrication techniques in CNSTs NanoFab at NIST. Similar with before, we also started from a silicon wafer with 3 μm thermal silicon dioxide layer. After the standard RCA clean, 730 nm thick silicon nitride film is deposited using low pressure chemical vapor deposition (LPCVD) and patterned by optical stepper lithography. SU8-2005 resist was used. After reactive-ion etching (RIE), the device is annealed at 1100℃ to break N-H bonds and then cladded and protected by LPCVD deposited silicon oxide. The width of

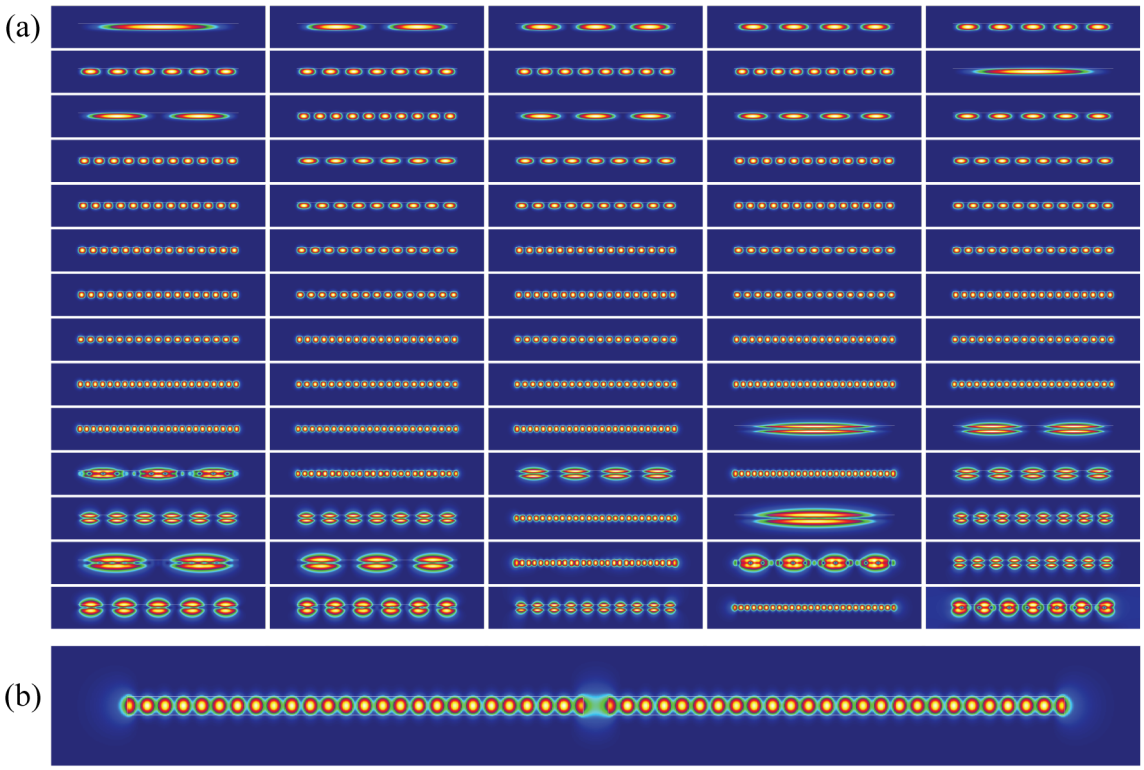

Figure 5.3: (a) A list of all 70 supported modes in the designed waveguide: including 37 TE modes and 33 TM modes. (b) The evanescent coupling between two waveguides separated by 1 μm.

waveguide in spiral structure is designed to be 18 μm, which can support as many as 37 TE modes and 33 TM modes according to the simulation results by FIMMWAVE. Figure 5.3(a) shows all the 70 supported modes in this designed waveguide dimension. The gap between the adjacent waveguides in the spiral is designed to be 1 μm, and from Figure 5.3(b) we can clearly see the cross talking between two waveguides separated by 1 μm, which will induce the evanescently coupling between the adjacent waveguide arms. The smallest bending radius in this device is 500 μm, and the total length of the cavity is 40 mm.

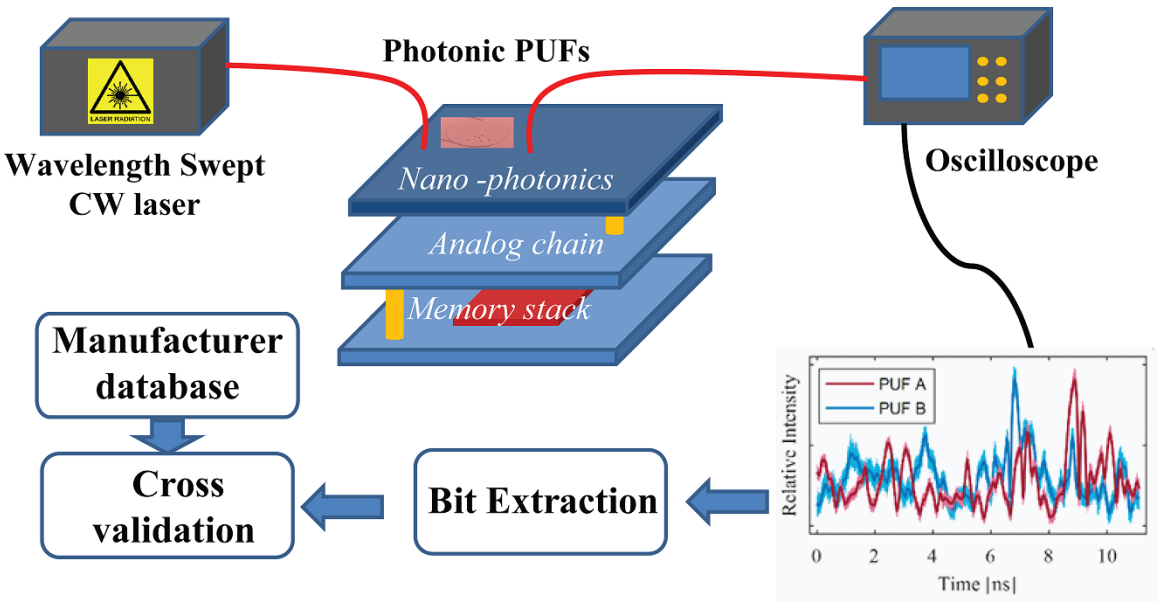

Figure 5.4: Tagging device validation system.

5.4 Validation System and Experimental Results

Figure 5.4 shows the scheme of our proposed tagging device validation system using our designed integrated photonic PUFs tagging on the electronic ICs. The measurement and validation techniques required for our scheme consist of characterizing a devices transmission spectrum using a wavelength tunable CW laser and an oscilloscope, providing a simple low-cost solution that can be readily incorporated into many stages of the electronics manufacturing supply chain. In a tagging application, validation can be performed based on the unique and complex transmission spectrum measured from the device. Correlation coefficient will be calculated against a manufacturers data base for validation.

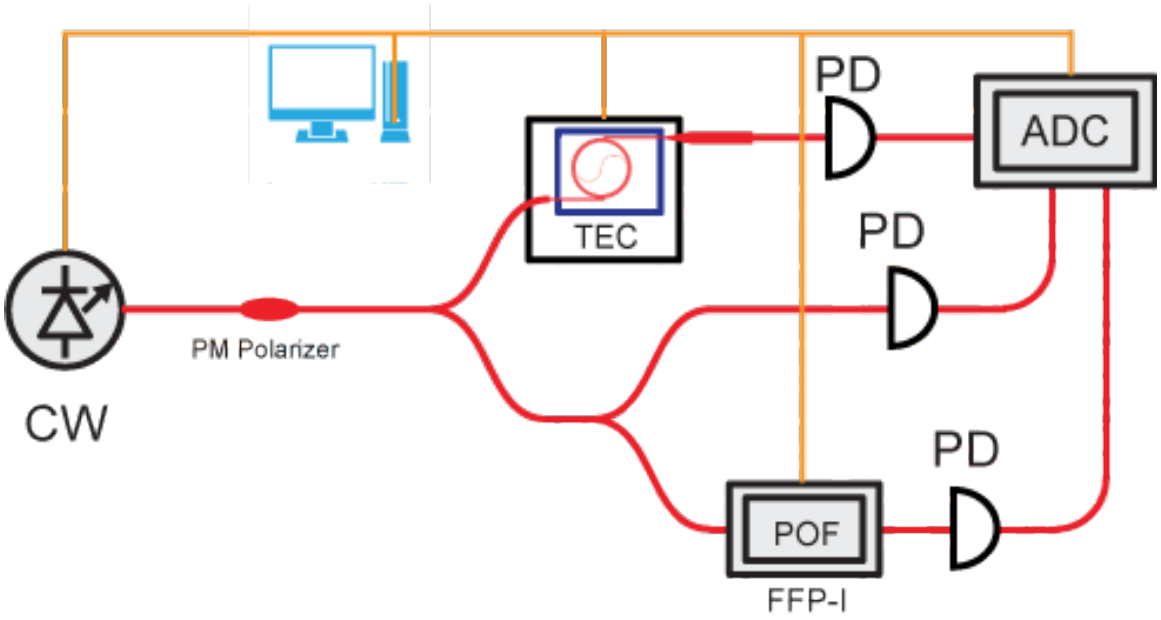

Figure 5.5: Experimental setup to measure the high resolution spectrum of the PUF device. FFP-I, Fiber Fabry-Perot Interferometer; PD, photodetector.

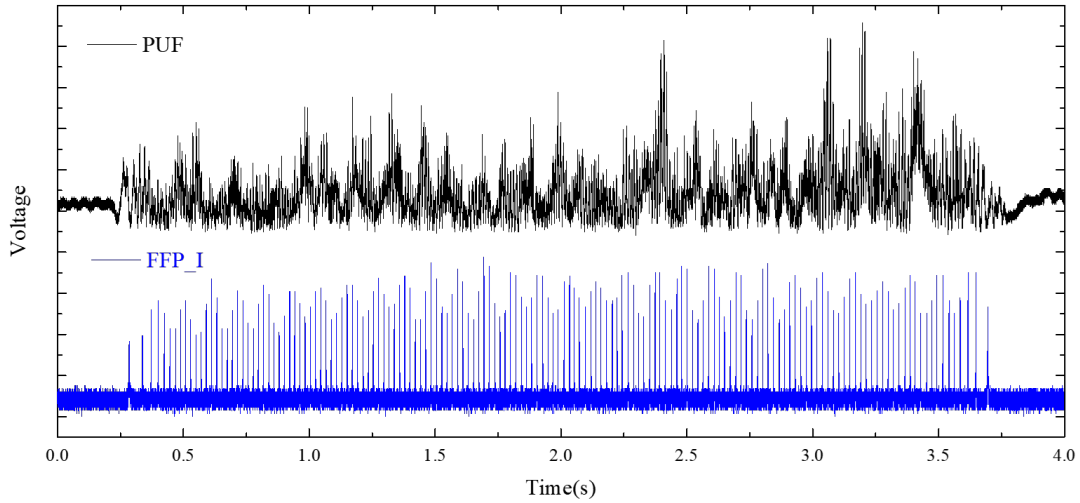

Figure 5.6: Example waveform of one device and the reference arm of FPP-I. FFP-I, Fiber Fabry-Perot Interferometer.

To validate the use of these devices as a secure unclonable ID in a tagging application we use the experimental setup shown in Figure 5.5. The continuous wave (CW) light source is wavelength swept from 1520 nm to 1570 nm at a speed of 15 nm/s. PM fiber is used to connect the laser to a collimator and guarantee the input polarization state the same. An in-line 70:30 PM fiber coupler is used to send 70% of the light into the photonic PUF device and the output is collected via a photodetector. The other 30% is divided into 2 reference arms: in one arm the input is sent directly to a photodetector for amplitude calibration, and in the other arm the input goes through a fiber Fabry-Perot interferometer (FFP-I) for wavelength calibration. The bandwidth of the FFP-I is 1.022 GHz and the free spectral range (FSR) is 39.87 GHz. One example output waveform collected by photodetector of the measured PUF device is shown in Figure 5.6(top); one example output waveform from the FFP-I reference arm is shown in Figure 5.6(bottom). Then the output waveform can be transformed to spectrum and calibrated based on the reference arms. The calibrated spectra are shown in Figure 5.7. The red curve shows the calibrated spectrum for a single photonic PUF device and the blue curve is the calibrated spectrum from that devices identical copy (attempted clone). The bottom figure in Figure 5.7 shows the zoom-in spectra from 1545 nm to 1555 nm. From the measurements, we can see that the output spectra is highly complex with a great number of features, and the output spectrum from the clone is completely uncorrelated.

The correlation coefficient r between two spectra A and B is calculated using the

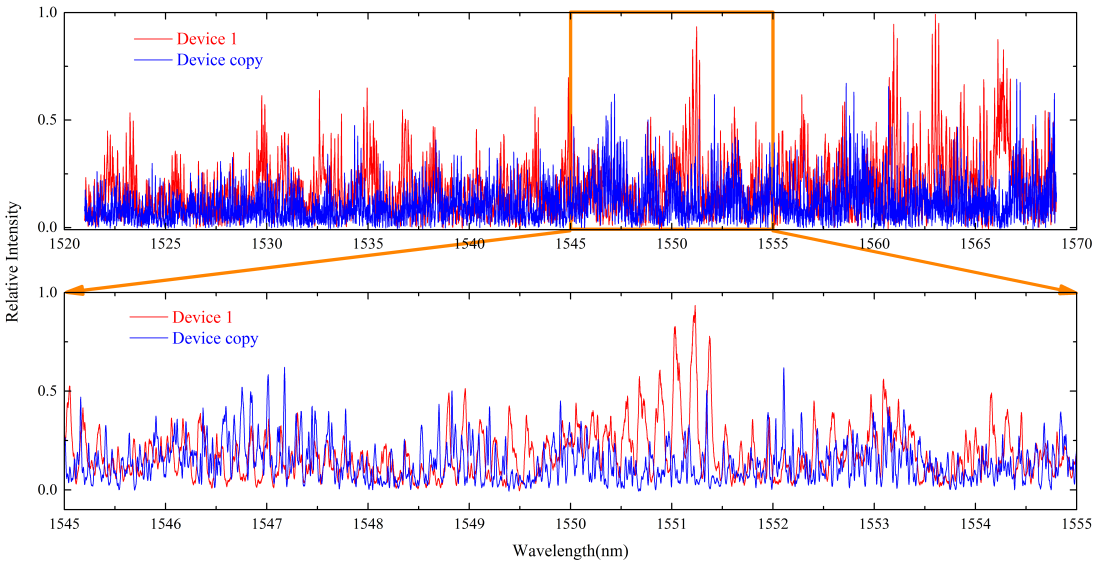

Figure 5.7: The top figure shows the calibrated high resolution spectra of one device (red curve) and its clone(blue curve). The bottom figure shows the zoom-in spectra ranging from 1545 nm to 1555 nm.

following equation:

$$r(A,B) = \frac{\sum_n (A_n - \bar{A})(B_n - \bar{B})}{\sqrt{\sum_n (A_n - \bar{A})^2 \sum_n (B_n - \bar{B})^2}} \ . \tag{5.1}$$

In equation 5.1, $\bar{A}$ and $\bar{B}$ are the mean values of A and B.The correlation coefficient between these two spectra is 0.0359, very close to 0, which proves that the two spectrum are completely uncorrelated. Despite these two devices have an identical design and being fabricated on the same wafer in the same processing run and they are located close to one another to ensure the similarity in fabrication conditions, each device exhibits distinct behavior due to slight fabrication variations such as sidewall roughness giving each device its own unique fingerprint.

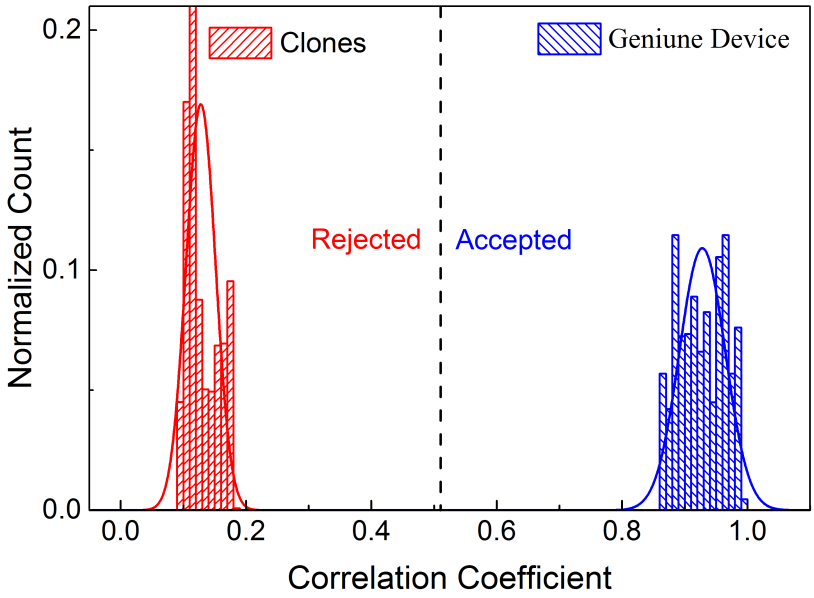

Figure 5.8: Correlation coefficient normal distribution and histograms between multiple measured output spectra of 4 devices that are clones of others.

The average of 24 measured output spectra of one device is stored as the manufacturer database. Validation is performed by calculating the correlation coefficient between the output spectra of testing device with the ground truth (the manufacturer database). Figure 5.8 shows the normalized histogram of the correlation coefficient distribution. The right blue histogram corresponds to the distribution of correlation coefficient between different measured output spectra of the same device, and the left red histogram is the distribution of correlation coefficient between the identical copies and the database. The separation between the same distribution and the copy distribution further demonstrates that even the optimally identical copy is clearly distinguishable. Furthermore, the center position of the copy distribution is close to

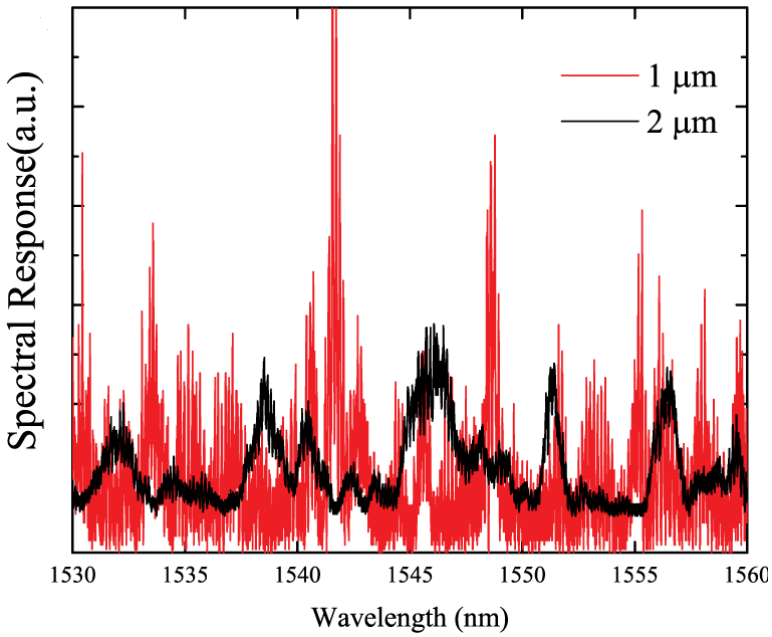

Figure 5.9: The output spectra of two devices with different gaps: 1 μm (red curve) and 2 μm (black curve).

0, which indicates very low correlation between the same device and the copy.

Moreover, Figure5.9 shows the output specta of two devices with 2 different gaps between adjacent waveguides. We can see that the spectral complexity can be enhanced by reducing the gap from 2 μm to 1 μm. The evanescent bi-directional coupling, as well as the extremely multimode natuer of the device make its response sensitive to the structural variations arising from the fabrication such as sidewall roughness and gap variation.

5.5 Temperature sensitivity test

As we can expect, this PUF device is highly sensitive to the enviremental temperature change. The refractive index of the waveguide and the gap between adjacent waveguides arm in the spiral structure will both change slightly due to the temperature change, and this will introduce a change to the coupling coefficient between the adjacent waveguides and then the change could be amplified due the chaotic design of the PUF. Figure 5.10 shows the comparison of the output spectra of with 0.5 ℃, 1.1 ℃ and 2.1 ℃ temperature difference, and the correlation coefficient as a function of the temperature difference. We can see that the output spectra of this photonics PUF is highly sensitive to the temperature as we expected. A temperature change of 1.1 ℃ causes a 35% decorrelation. However, there are existing temperature controllers that can supply sufficient temperature stability for this photonics PUF to operate. Alternately, the PUF can possibly be operated at multiple temperatures for different authentications.

5.6 Packaging and Repeatability Test

Finally, we perform an over-time repeatability test to determine the overall stability of the test system. Since the photonics PUF spectral response might be sensitive to the input coupling conditions, we package the chip with one PM fiber coupled to one waveguide on the chip as shown in the Figure 5.11(a). A clear UV curable adhe-

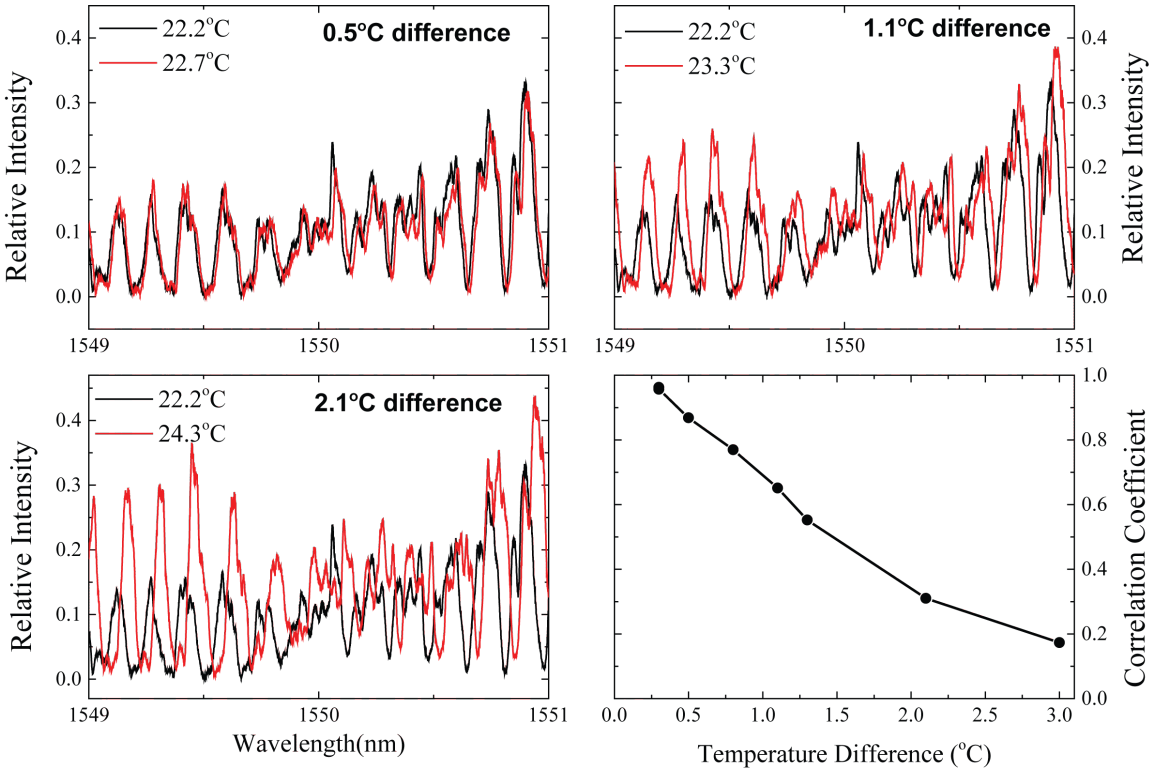

Figure 5.10: The comparison of output spectra of with varying temperature difference, and the correlation coefficient as a function of the temperature difference.

sive (Dymax OP-4-20632-GEL) adhesive is applied in between. The input coupling loss is estimated to be -10 dB due to the mismatch between the cross-section sizes of the PM fiber and the waveguide. Furthermore, the temperature is maintained at 23℃ using a temperature controller and the polarization to be in the cross-polarized state using a PM fiber polarizer and a fiber rotator. Figure 5.11(b). shows the correlation coefficient between two output spectra from the same device with the time difference from 3 days to 10 days. A broadband light source from the amplified spontaneous emission (ASE) of an erbium doped fiber amplifier (EDFA) is sent into the device and the output spectra are collected using an optical spectrum analyzer (OSA). We can see that the correlation coefficient has been maintained on a high level (around 0.97) during this time period, which clearly indicates a good repeatability of the system over time. We expect that a system with other components integrated into the chip will further improve the stability of the system.

5.7 Conclusion

In summary, we fabricate an on-chip photonic PUF using spiral waveguides formed in silicon nitride. We demonstrate that this photonic PUF cannot be cloned and can be well distinguished from its clones from the correlation distribution histogram. We also investigate the temperature sensitivity and over-time long term repeatability of this device. We believe that this PUF can be used for an identification tagging

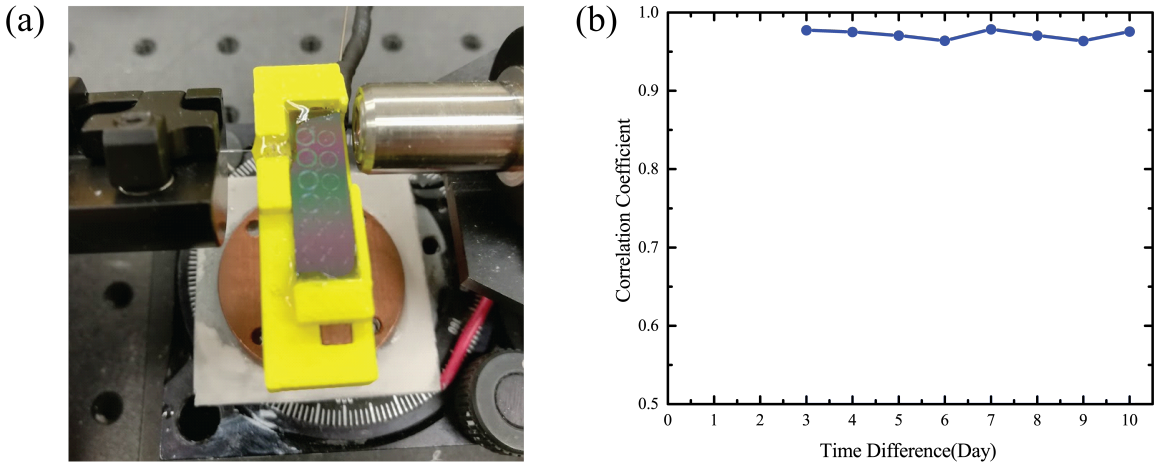

Figure 5.11: (a) Photograph of packaged chip with one PM fiber coupled to one waveguide device. (b) The correlation coefficient between two output spectra with the time difference from 3 days to 10 days.

application for electronic ICs.

Chapter 6

Compressed Sensing of Sparse RF Signals Based on Silicon Photonic Microcavities

6.1 Introduction

Todays Radio frequency environment is very congested, but the actual usage of the RF domain is sparse at any given location and time, which means that the RF spectrum is greatly underutilized.It is therefore very important to monitor spectral usage rapidly in order to best serve all the users that are sharing a given radio channel. As a result, emerging radio technologies, such as cognitive radio, aim to better use the available spectrum through dynamic allocation and rapid spectrum sensing is a

critical technology for this vision.Cognitive radio need s to decide if a frequency band is available for communication at a given time. Also the demand of the spectrum sensing bandwidth keeps increasing. On July 2016, FCC approved the RF spectrum for 5G including 28 GHz, 37GHz and 39GHz bands. That means the wireless system is moving to the higher frequency bands, which typically will involve with larger bandwidth. At higher frequency, direct Nyquist sampling becomes more difficult and definitely more expensive. To this end, compressive sensing (CS) has been applied for the rapid measurement of sparse radio frequency spectra using both electronic and photonic systems [49–51]. Compared with electronic CS, photonic CS can provide much greater sensing bandwidth.

6.2 Compressed Sensing

As mentioned before, Nyquist sampling is not the most efficient way of measuring the RF spectrum. Most real signals are band-limited and sparse in the frequency domain, which means it is suitable for compressed sensing. In CS systems, an unknown signal of dimension N can be characterized using a sub-Nyquist number of measurements M which is less than dimension N. The measurements are typically formed from the vector inner product between the unknown signal and a set of M

pseudorandom patterns as in this equation:

$$y_k = \langle x, \phi_k \rangle , \qquad k = 1 \dots M, \tag{6.1}$$

where x is a sparse signal, ϕ_{k} is one applied pseudorandom pattern and $\mathrm{y_k}$ is one compressed sensing measurement; k is up to M, in which usually M $\ll$ N. Using certain algorithm, we can find the sparest solutions and reconstruct the signal based on these M measurements and the full knowledge of the random patterns. If the input signal is sparse, the required acquisition number M will be much less than Nyquist sampling number N, and M/N is defined as compression ratio. In a CS system, the signal can be reconstructed with a lower sampling rate and fewer measurements. As we can see that the pseudorandom pattern generator is critical to the CS system, but it often requires a high-speed electronics for the measurement of ultrawide-bandwidth signals.

6.3 Photonic compressed sensing

Compressed sensing has already been applied for the rapid measurement of sparse RF signal in electronic systems. With an increasing signal bandwidth, electronic CS systems require expensive high-speed analog electronics. Photonic CS system has the potential to provide much larger sensing bandwidth. Our group previously developed one photonic CS system [49] by using a chirped pulse stretched in time

using dispersion compensating fibers. Both the location and amplitude of the input RF frequencies can be reconstructed using ¡1% of the measurements required for Nyquist sampling. However, this system still requires a high-speed electronics for the measurement of ultra-wide-bandwidth signals.

Recently, alternatives to direct patterning such as multiple scattering [52] and multimode waveguide interference [53] were proposed as a way to generate the pseudorandom CS sensing matrix without the need for high-speed electronics and optoelectronics. Our previous work has developed on-chip chaotic multimode microcavities that possess unique spectral fingerprints [47] due to the randomness of cavity surface or sidewall and the chaotic resonances of the cavity. We have shown that even cavities with identical design will possess distinct spectral and temporal behaviors. Here, we demonstrate the use of these devices to generate random spectral patterns for compressive measurement of radio frequency spectra with small size, weight and reduced power requirements.

6.4 Device design and Fabrication

Figure 6.1(a) presents the SEM image of one silcon PUF device. As shown in this figure, the device consists of highly multi-mode chamfered disk made of single-crystal silicon whose input and output consist of single mode silicon waveguides. The chamfer is implemented such that the cavities exhibit ray chaotic behavior for the reverber-

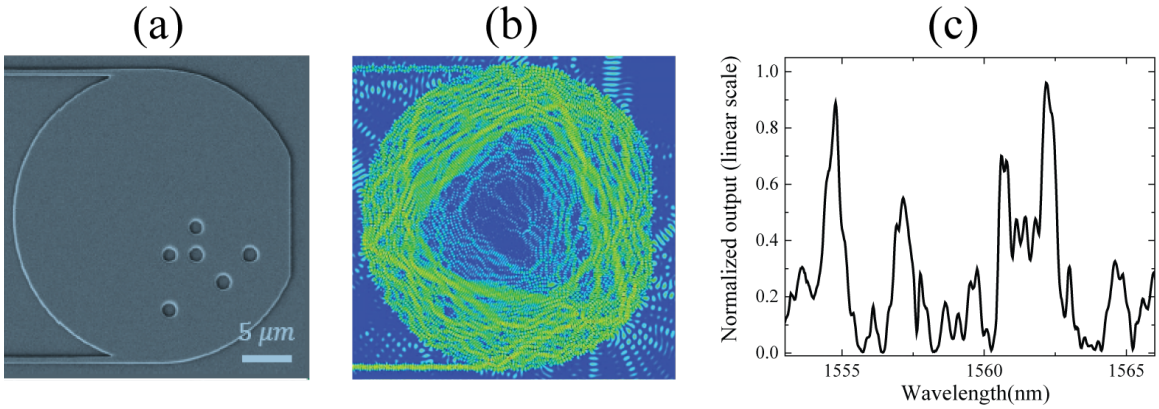

Figure 6.1: (a) SEM image of one silcon PUF device. (b) A finite difference time domain (FDTD) image detailing the excitation of many transient optical modes within the cavity after ultrafast excitation. (c) Unique pseudorandom transmission spectrum from one cavity device.

ating lightwaves. The device has a silicon thickness of 220 nm and an approximate diameter of 60 μm. Figure 6.1(b) presents a finite difference time domain (FDTD) image detailing the excitation of many transient optical modes within the cavity after ultrafast excitation. This cavity can excite hundreds of modes, it has unique fingerprints due to the chaotic resonances of the cavity and randomness of cavity surface or sidewall. These devices can be used as physical unclonable function. Because of the unique cavity fingerprint, this device is ideal to work as a Pseudorandom pattern generator in compressed sensing. Figure 6.1(c) presents unique pseudorandom transmission spectrum from one cavity device.

We fabricate the silicon chaotic microcavities in CNSTs NanoFab at NIST using standard microelectronics fabrication techniques. We began device fabrication with silicon-on-insulator wafers with a 3 μm thick buried oxide layer and 500 nm thick top silicon layer. The top silicon layer is thinned down to a thickness of 220 nm

by growing thermal oxide on the silicon surface and removing it with hydrofluoric acid etching. This thinning process took place in two stages and during the second stage approximately 100 nm of thermal oxide was left on the surface to serve as an etch mask in later steps. A JEOL-6300 electron beam lithography system was used to write the pattern. MaN-2405 served as a mask when we etched the pattern into the thermal oxide layer via reactive ion etching (RIE). This oxide layer then served as a hard mask for etching the pattern into the silicon layer via inductively-coupled plasma (ICP) etching. In the end, we cladded the resulting silicon waveguides with 1 μm of silicon dioxide via PECVD.

6.5 Experimental setup

The experimental setup for CS radio frequency measurement is presented in Figure 6.2. Ultrafast 300-fs pulses from a 90-MHz mode-locked laser (MLL) are first chirped using dispersion compensating fiber (DCF, D=-247 ps/nm) with normal dispersion to stretch the pulse to several nanoseconds in time. The pulses are then sent through a Mach-Zehnder modulator (MZM) to imprint the RF signal of interest onto the optical intensity as a function of time. Since the pulses are highly chirped this temporal modulation likewise imprints the RF signal of interest onto the optical spectrum of each pulse. Then the pulses pass through dispersion compensating fiber to compress the pulse back to a relatively narrow temporal duration for high signal-to-noise ratio

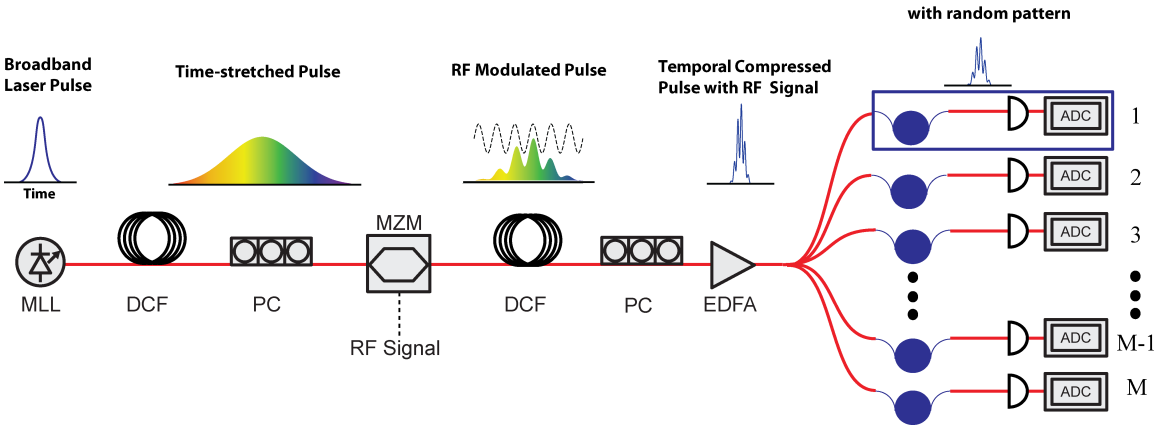

Figure 6.2: Experimental setup of the compressed sensing system using silicon chaotic cavities as the pseudorandom pattern generators.

(SNR) output photo detection with a synchronized ADC. The pulses are amplified and input to 8 different micro cavities with 3 different polarization states (TE, TM and cross polarization). The un-modulated optical spectra from each device and polarization are characterized with an optical spectrum analyzer (OSA) to create the CS sensing matrix; the compressed measurements are acquired from the total power received after passing the RF modulated pulses though each device.

These chaotic cavities work as integrated pseudorandom filter bank. These M=24 measurements can operate in parallel at a slow rate, which is only 2/N of the RF bandwidth. By using this approach, the resource is saved at the ratio of M/N, which is much less than 1.

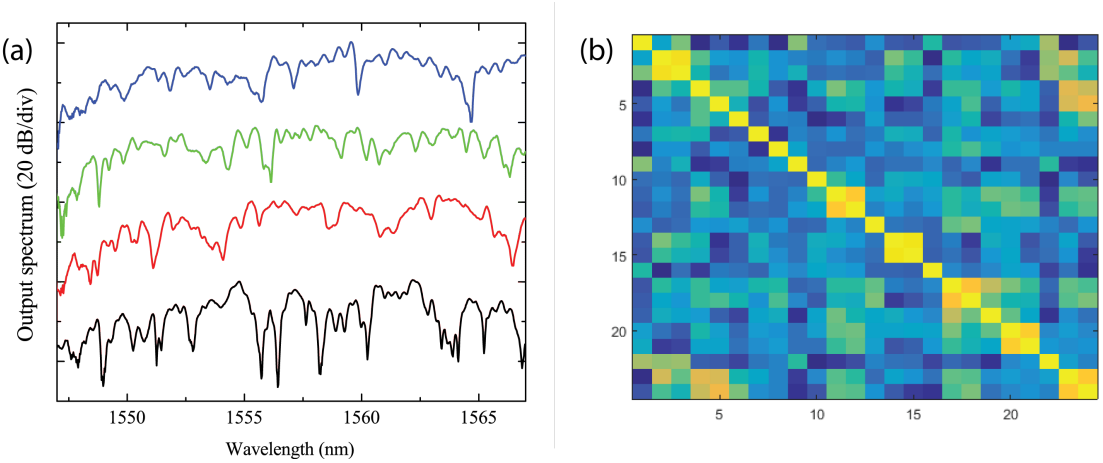

Figure 6.3: (a) The output spectra of 4 different devices. (b) Correlation plot of 24 pseudorandom patterns generated by micro cavities.

6.6 Experimental results

Figure 6.3(a) shows the output spectra of 4 different example chaotic microcavities. As is shown, these spectra present random and uncorrelated features ideal for CS measurement. The minimal feature size of the output spectra is equivalent to about 71 ps temporal feature size. We also calculate the normalized cross-correlation among all of 24 random illumination patterns, and the result is shown in Figure 6.3(b). We can see that the correlation between the unlike patterns is relatively low.

By using these 24 random patterns, we successfully demonstrate accurate reconstructions of the amplitude of a single RF tone derived from the MLL (64th harmonic). Figure 6.4(a) shows all the compressed signal levels of M=24 measurements. In Figure 6.4(b), the tone at 5.76 GHz was reconstructed onto a grid with N=300 frequency bins, set by the overall width and resolution of the measured spectral response of the microcavities to the MLL spectrum. A compression ratio of 8% (M/N) is achieved

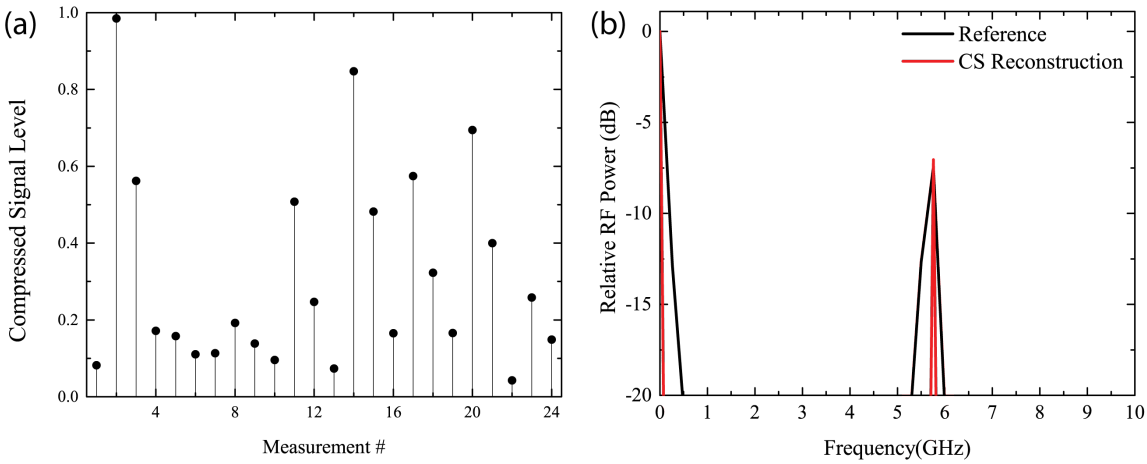

Figure 6.4: (a) Compressed signal level of M=24 measurements. (B) One tone reconstruction of RF signal at 5.76 GHz with N=300 frequency bins by using 24 random patterns.

in this case. We reconstruct the RF signal with 8% of the measurements required by Nyquist sampling and at only 1/150 of the Nyquist sampling rate.

6.7 Conclusion

To sum up, by using these 24 random patterns, we successfully demonstrate accurate reconstructions of the amplitude of a single RF tone derived from the MLL (64th harmonic). The tone at 5.76 GHz was reconstructed onto a grid with N=300 frequency bins, set by the overall width and resolution of the measured spectral response of the microcavities to the MLL spectrum. A compression ratio of 8% (M/N) is achieved in this case.

Chapter 7

Conclusion and future work

7.1 Conclusion

This dissertation includes the background and three different silicon based platforms: Crystalline silicon (c-Si), hydrogenate amorphous silicon (a-Si:H) and silicon nitride (Si_3N_4). Based on these 3 different material platform, 5 different demonstrations are discussed:

(1) Phase-sensitive amplification demonstration in a-Si:H waveguides. We experimentally demonstrate phase-sensitive amplification based on pump-degenerate FWM in a-Si:H waveguides under 90-MHz and 10-GHz pulsed operation. At 90 MHz, a maximum extinction ratio of 11.7 dB is achieved with 1.6 W peak pump power. Due to the high nonlinearity and nonlinear figure of merit in a-Si:H, we are able to achieve a 6.6 dB extinction ratio at 0.5 W peak pump

power at 10 GHz. This is obtained at this communication data rate without any attempt to mitigate the effects of nonlinear loss mechanisms (such as a p-i-n diode structure for carrier removal). We also demonstrate phase-sensitive operation in this waveguide at continuous-wave operation of 1.6-dB ER with an input power of 38 mW. This platform is backend compatible with CMOS fabrication processing and has the potential to enable on-chip all-optical phase and amplitude regeneration.

(2) Mid-IR supercontinuum generation in a-Si:H waveguides. We successfully demonstrate a 790 nm wide Mid-IR supercontinuum generation, spanning from 1.63 μm to 2.42 μm, using a femtosecond pulsed pump Thulium-dosed fiber laser centered at 1910 nm in a hydrogenated amorphous silicon waveguide.

(3) Optical frequency combs in high-Q silicon nitride ring resonators. We successfully fabricated silicon nitride micro-ring resonators with a Q factor as high as 1.7 million. The propagation loss achieves as low as 0.13 dB/cm. By tuning a continuous wave laser into the resonance of the micro-ring resonator, a parametric amplification occurs and optical frequency combs over a bandwidth of more than 240 nm is achieved.

(4) Photonic physical unclonable functions using silicon nitride spiral waveguides. On-chip photonic PUF using spiral waveguides based on silicon nitride is fabricated. We demonstrate that this photonic PUF cannot be cloned and can be

well distinguished from its clones from the FHD histogram. We also investigate the temperature sensitivity and over-time repeatability of this device. We believe that this PUF can be used for an identification tagging application for electronic ICs.

(5) Compressed sensing of sparse RF signals based on silicon microdisk. By using these 24 random patterns, we successfully demonstrate accurate reconstructions of the amplitude of a single RF tone derived from the MLL (64th harmonic). The tone at 5.76 GHz was reconstructed onto a grid with N=300 frequency bins, set by the overall width and resolution of the measured spectral response of the microcavities to the MLL spectrum. A compression ratio of 8% (M/N) is achieved in this case.

7.2 Furture work

We have shown the CS demonstration using silicon microcavities. We will continue to study compressed sensing of sparse RF signals based silicon nitride spiral cavities. The limitation of the silicon photonic cavities for compressed sensing application is that the high nonlinearity of crystalline silicon makes the measurement sensitive to the power level of the input sparse RF signals. However, the nonlinearity of silicon nitride is one order smaller than crystalline silicon, which makes the device less sensitive to the power levels. Moreover, we can design a silicon nitride spiral cavity with multiple

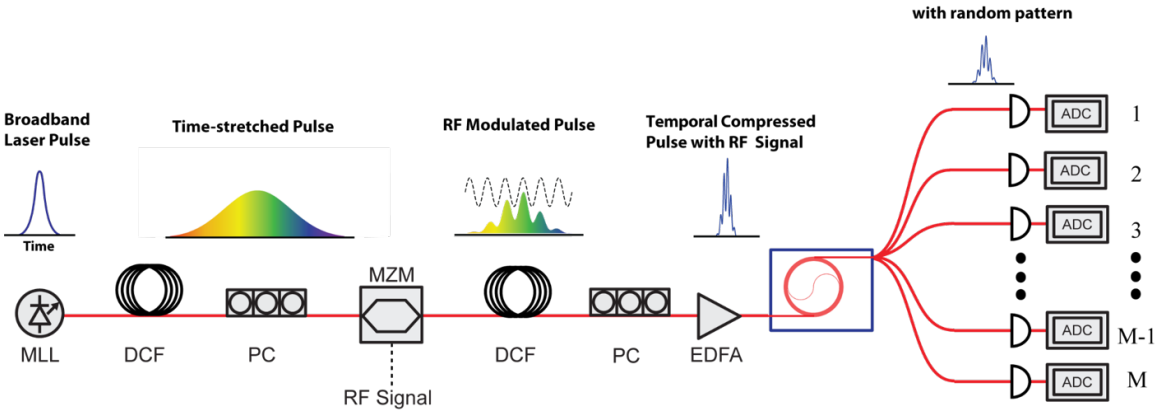

Figure 7.1: Proposed experimental setup of the CS system based silicon nitride PUF devices.

outputs as shown in Figure 7.1. Each output works as one pseudorandom pattern generator and then decrease the required number of devices.

Bibliography

[1] G. E. Moore, "Progress in digital integrated electronics [technical literaiture, copyright 1975 ieee. reprinted, with permission. technical digest. international electron devices meeting, ieee, 1975, pp. 11-13.]," *IEEE Solid-State Circuits Society Newsletter*, vol. 20, no. 3, 2006.

[2] A. Alduino and M. Paniccia, "Interconnects: Wiring electronics with light," *Nature Photonics*, vol. 1, no. 3, p. 153, 2007.

[3] N. Izhaky, M. T. Morse, S. Koehl, O. Cohen, D. Rubin, A. Barkai, G. Sarid, R. Cohen, and M. J. Paniccia, "Development of cmos-compatible integrated silicon photonics devices," *IEEE Journal of selected topics in quantum electronics*, vol. 12, no. 6, pp. 1688–1698, 2006.

[4] R. Soref and J. Lorenzo, "Single-crystal silicon: a new material for 1.3 and 1.6 μm integrated-optical components," *Electronics Letters*, vol. 21, no. 21, pp. 953–954, 1985.

[5] G. T. Reed, W. R. Headley, and C. J. Png, "Silicon photonics: The early years,"

in *Optoelectronic Integration on Silicon II*, vol. 5730. International Society for Optics and Photonics, 2005, pp. 1–19.

[6] A. Rickman, "The commercialization of silicon photonics," *Nature Photonics*, vol. 8, no. 8, p. 579, 2014.

[7] M. Dinu, F. Quochi, and H. Garcia, "Third-order nonlinearities in silicon at telecom wavelengths," *Applied physics letters*, vol. 82, no. 18, pp. 2954–2956, 2003.

[8] B. Kuyken, S. Clemmen, S. K. Selvaraja, W. Bogaerts, D. Van Thourhout, P. Emplit, S. Massar, G. Roelkens, and R. Baets, "On-chip parametric amplification with 26.5 db gain at telecommunication wavelengths using cmos-compatible hydrogenated amorphous silicon waveguides," *Optics letters*, vol. 36, no. 4, pp. 552–554, 2011.

[9] B. Kuyken, H. Ji, S. Clemmen, S. K. Selvaraja, H. Hu, M. Pu, M. Galili, P. Jeppesen, G. Morthier, S. Massar *et al.*, "Nonlinear properties of and nonlinear processing in hydrogenated amorphous silicon waveguides," *Optics express*, vol. 19, no. 26, pp. B146–B153, 2011.

[10] K.-Y. Wang and A. C. Foster, "Ultralow power continuous-wave frequency conversion in hydrogenated amorphous silicon waveguides," *Optics letters*, vol. 37, no. 8, pp. 1331–1333, 2012.

[11] R. Slavík, F. Parmigiani, J. Kakande, C. Lundström, M. Sjödin, P. A. Andrekson, R. Weerasuriya, S. Sygletos, A. D. Ellis, L. Grüner-Nielsen *et al.*, "All-optical phase and amplitude regenerator for next-generation telecommunications systems," *Nature Photonics*, vol. 4, no. 10, p. 690, 2010.

[12] Z. Tong, C. Lundström, P. Andrekson, C. McKinstrie, M. Karlsson, D. Blessing, E. Tipsuwannakul, B. Puttnam, H. Toda, and L. Grüner-Nielsen, "Towards ultrasensitive optical links enabled by low-noise phase-sensitive amplifiers," *Nature Photonics*, vol. 5, no. 7, p. 430, 2011.

[13] R. Neo, J. Schröder, Y. Paquot, D.-Y. Choi, S. Madden, B. Luther-Davies, and B. J. Eggleton, "Phase-sensitive amplification of light in a χ (3) photonic chip using a dispersion engineered chalcogenide ridge waveguide," *Optics express*, vol. 21, no. 7, pp. 7926–7933, 2013.

[14] A. Willinger, A. Martin, S. Combrié, A. De Rossi, and G. Eisenstein, "Phase sensitive parametric interactions in a $ga\_\{0.5\}in\_\{0.5\}p$ photonic crystal waveguide," *IEEE Photonics Journal*, vol. 8, no. 5, pp. 1–7, 2016.

[15] F. Da Ros, M. Pu, L. Ottaviano, H. Hu, E. Semenova, M. Galili, K. Yvind, L. Oxenl *et al.*, "Phase-sensitive four-wave mixing in algaas-on-insulator nanowaveguides," in *Photonics Conference (IPC), 2016 IEEE*. IEEE, 2016, pp. 505–506.

[16] Y. Zhang, C. Husko, J. Schröder, S. Lefrancois, I. H. Rey, T. F. Krauss, and B. J.

Eggleton, "Phase-sensitive amplification in silicon photonic crystal waveguides," *Optics letters*, vol. 39, no. 2, pp. 363–366, 2014.

[17] J. Leuthold, C. Koos, and W. Freude, "Nonlinear silicon photonics," *Nature Photonics*, vol. 4, no. 8, p. 535, 2010.

[18] F. Da Ros, D. Vukovic, A. Gajda, K. Dalgaard, L. Zimmermann, B. Tillack, M. Galili, K. Petermann, and C. Peucheret, "Phase regeneration of dpsk signals in a silicon waveguide with reverse-biased pin junction," *Optics express*, vol. 22, no. 5, pp. 5029–5036, 2014.

[19] M. A. Ettabib, K. Bottrill, F. Parmigiani, A. Kapsalis, A. Bogris, M. Brun, P. Labeye, S. Nicoletti, K. Hammani, D. Syvridis *et al.*, "All-optical phase regeneration with record psa extinction ratio in a low-birefringence silicon germanium waveguide," *Journal of Lightwave Technology*, vol. 34, no. 17, pp. 3993–3998, 2016.

[20] H. A. Haus and J. Mullen, "Quantum noise in linear amplifiers," *Physical Review*, vol. 128, no. 5, p. 2407, 1962.

[21] J. Kakande, F. Parmigiani, M. Ibsen, P. Petropoulos, and D. J. Richardson, "Wide bandwidth experimental study of nondegenerate phase-sensitive amplifiers in single-and dual-pump configurations," *IEEE Photonics Technology Letters*, vol. 22, no. 24, pp. 1781–1783, 2010.

[22] Y. Zhang, J. Schröder, C. Husko, S. Lefrancois, D.-Y. Choi, S. Madden, B. Luther-Davies, and B. J. Eggleton, "Pump-degenerate phase-sensitive amplification in chalcogenide waveguides," *JOSA B*, vol. 31, no. 4, pp. 780–787, 2014.

[23] J. M. Dudley, G. Genty, and S. Coen, "Supercontinuum generation in photonic crystal fiber," *Reviews of modern physics*, vol. 78, no. 4, p. 1135, 2006.

[24] M. R. Lamont, B. Luther-Davies, D.-Y. Choi, S. Madden, and B. J. Eggleton, "Supercontinuum generation in dispersion engineered highly nonlinear (γ= 10/w/m) as 2 s 3 chalcogenide planar waveguide," *Optics Express*, vol. 16, no. 19, pp. 14 938–14 944, 2008.

[25] R. Halir, Y. Okawachi, J. Levy, M. Foster, M. Lipson, and A. Gaeta, "Ultra-broadband supercontinuum generation in a cmos-compatible platform," *Optics letters*, vol. 37, no. 10, pp. 1685–1687, 2012.

[26] C. Phillips, C. Langrock, J. Pelc, M. Fejer, J. Jiang, M. E. Fermann, and I. Hartl, "Supercontinuum generation in quasi-phase-matched linbo 3 waveguide pumped by a tm-doped fiber laser system," *Optics letters*, vol. 36, no. 19, pp. 3912–3914, 2011.

[27] B. Kuyken, X. Liu, R. M. Osgood, R. Baets, G. Roelkens, and W. M. Green, "Mid-infrared to telecom-band supercontinuum generation in highly nonlinear

silicon-on-insulator wire waveguides," *Optics Express*, vol. 19, no. 21, pp. 20 172–20 181, 2011.

[28] U. D. Dave, S. Uvin, B. Kuyken, S. Selvaraja, F. Leo, and G. Roelkens, "Telecom to mid-infrared spanning supercontinuum generation in hydrogenated amorphous silicon waveguides using a thulium doped fiber laser pump source," *Optics express*, vol. 21, no. 26, pp. 32 032–32 039, 2013.

[29] F. Leo, J. Safioui, B. Kuyken, G. Roelkens, and S.-P. Gorza, "Generation of coherent supercontinuum in a-si: H waveguides: experiment and modeling based on measured dispersion profile," *Optics express*, vol. 22, no. 23, pp. 28 997–29 007, 2014.

[30] J. Safioui, F. Leo, B. Kuyken, S.-P. Gorza, S. K. Selvaraja, R. Baets, P. Emplit, G. Roelkens, and S. Massar, "Supercontinuum generation in hydrogenated amorphous silicon waveguides at telecommunication wavelengths," *Optics express*, vol. 22, no. 3, pp. 3089–3097, 2014.

[31] B. Kuyken, T. Ideguchi, S. Holzner, M. Yan, T. W. Hänsch, J. Van Campenhout, P. Verheyen, S. Coen, F. Leo, R. Baets *et al.*, "An octave-spanning mid-infrared frequency comb generated in a silicon nanophotonic wire waveguide," *Nature communications*, vol. 6, p. 6310, 2015.

[32] T. Udem, R. Holzwarth, and T. W. Hänsch, "Optical frequency metrology," *Nature*, vol. 416, no. 6877, p. 233, 2002.

[33] A. Schliesser, M. Brehm, F. Keilmann, and D. W. van der Weide, "Frequency-comb infrared spectrometer for rapid, remote chemical sensing," *Optics Express*, vol. 13, no. 22, pp. 9029–9038, 2005.

[34] S. A. Diddams, L. Hollberg, and V. Mbele, "Molecular fingerprinting with the resolved modes of a femtosecond laser frequency comb," *Nature*, vol. 445, no. 7128, p. 627, 2007.

[35] P. DelHaye, A. Schliesser, O. Arcizet, T. Wilken, R. Holzwarth, and T. J. Kippenberg, "Optical frequency comb generation from a monolithic microresonator," *Nature*, vol. 450, no. 7173, p. 1214, 2007.

[36] Y. Okawachi, K. Saha, J. S. Levy, Y. H. Wen, M. Lipson, and A. L. Gaeta, "Octave-spanning frequency comb generation in a silicon nitride chip," *Optics letters*, vol. 36, no. 17, pp. 3398–3400, 2011.

[37] A. A. Savchenkov, A. B. Matsko, D. Strekalov, M. Mohageg, V. S. Ilchenko, and L. Maleki, "Low threshold optical oscillations in a whispering gallery mode c a f 2 resonator," *Physical review letters*, vol. 93, no. 24, p. 243905, 2004.

[38] C. Y. Wang, T. Herr, P. DelHaye, A. Schliesser, J. Hofer, R. Holzwarth, T. Hänsch, N. Picqué, and T. J. Kippenberg, "Mid-infrared optical frequency combs at 2.5 μm based on crystalline microresonators," *Nature communications*, vol. 4, p. 1345, 2013.

[39] A. Gondarenko, J. S. Levy, and M. Lipson, "High confinement micron-scale silicon nitride high q ring resonator," *Optics express*, vol. 17, no. 14, pp. 11 366–11 370, 2009.

[40] K. Luke, A. Dutt, C. B. Poitras, and M. Lipson, "Overcoming si 3 n 4 film stress limitations for high quality factor ring resonators," *Optics Express*, vol. 21, no. 19, pp. 22 829–22 833, 2013.

[41] U. Guin, K. Huang, D. DiMase, J. M. Carulli, M. Tehranipoor, and Y. Makris, "Counterfeit integrated circuits: A rising threat in the global semiconductor supply chain," *Proceedings of the IEEE*, vol. 102, no. 8, pp. 1207–1228, 2014.

[42] U. Rührmair and J. Sölter, "Puf modeling attacks: An introduction and overview," in *Proceedings of the conference on Design, Automation & Test in Europe*. European Design and Automation Association, 2014, p. 348.

[43] R. Pappu, B. Recht, J. Taylor, and N. Gershenfeld, "Physical one-way functions," *Science*, vol. 297, no. 5589, pp. 2026–2030, 2002.

[44] R. Horstmeyer, B. Judkewitz, C. Yang, and I. M. Vellekoop, "Physical key-protected one time pad," Jun. 9 2015, uS Patent 9,054,871.

[45] B. R. Anderson, R. Gunawidjaja, and H. Eilers, "Initial tamper tests of novel tamper-indicating optical physical unclonable functions," *Applied optics*, vol. 56, no. 10, pp. 2863–2872, 2017.

[46] G. C. Birch, B. L. Woo, C. F. LaCasse, J. J. Stubbs, and A. L. Dagel, "Computational optical physical unclonable functions," in *Security Technology (ICCST), 2017 International Carnahan Conference on.* IEEE, 2017, pp. 1–6.

[47] B. C. Grubel, B. T. Bosworth, M. R. Kossey, H. Sun, A. B. Cooper, M. A. Foster, and A. C. Foster, "Silicon photonic physical unclonable function," *Optics Express*, vol. 25, no. 11, pp. 12 710–12 721, 2017.

[48] B. Redding, S. F. Liew, Y. Bromberg, R. Sarma, and H. Cao, "Evanescently coupled multimode spiral spectrometer," *Optica*, vol. 3, no. 9, pp. 956–962, 2016.

[49] B. T. Bosworth and M. A. Foster, "High-speed ultrawideband photonically enabled compressed sensing of sparse radio frequency signals," *Optics letters*, vol. 38, no. 22, pp. 4892–4895, 2013.

[50] J. Nichols and F. Bucholtz, "Beating nyquist with light: a compressively sampled photonic link," *Optics Express*, vol. 19, no. 8, pp. 7339–7348, 2011.

[51] G. C. Valley, G. A. Sefler, and T. J. Shaw, "Photonic technologies for undersampling and compressive sensing of high-speed rf signals," in *Optical Fiber Communications Conference and Exhibition (OFC), 2016.* IEEE, 2016, pp. 1–3.

[52] J. Shin, B. T. Bosworth, and M. A. Foster, "Single-pixel imaging using com-

pressed sensing and wavelength-dependent scattering," *Optics letters*, vol. 41, no. 5, pp. 886–889, 2016.

[53] G. C. Valley, G. A. Sefler, and T. J. Shaw, "Multimode waveguide speckle patterns for compressive sensing," *Optics letters*, vol. 41, no. 11, pp. 2529–2532, 2016.

Vita

Hongcheng Sun graduated from Nanjing University in China with a B.S.(2008) and M.S.(2011) in physics department, respectively. After that, he enrolled in department of electrical and computer engineering at Johns Hopkins University. He acquired a M.S. degree (2014) from this department and continues pursuing a PhD. During his PhD study, his research work focuses on optical communication and information secure applications in silicon photonics. His work appears in Optics Letters and Optics Express. He has given 5 conference talks during his PhD study.